Improvement on Generalized Finite Element Method by Identifying the Optimal Configuration of Enrichment Functions

Naier Mahdinejadgargari

Advisor: Prof. Ricardo Luiz da Silva Adriano

Co- Advisor: Prof. Hilton de Oliveira Mota

Belo Horizonte, February, 2019

Naier Mahdienjadgargari

Improvement on Generalized Finite Element Method by Identifying the Optimal Configuration of Enrichment Functions

This work is presented to the Program of Graduate Studies in Electrical Engineering (PPGEE) of Federal University of Minas Gerais to obtain a PhD degree in Electrical Engineering.

Concentration Area: Applied Electromagnetics

Supervisor: Prof. Dr. Ricardo Luiz da Silva Adriano

Co-Supervisor: Prof. Dr. Hilton de Oliveira Mota

Federal University of Minas Gerais

Belo Horizonte

Engineering School of UFMG

2019

"Improvement On Generalized Finite Element Method By Identifying The Optimal Configuration Of Enrichment Functions"
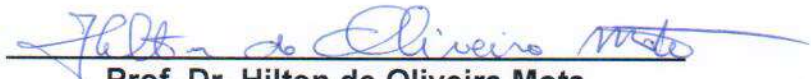
Naier Mahdinejadgargari

Tese de Doutorado submetida à Banca Examinadora designada pelo Colegiado do Programa de Pós-Graduação em Engenharia Elétrica da Escola de Engenharia da Universidade Federal de Minas Gerais, como requisito para obtenção do grau de Doutor em Engenharia Elétrica.
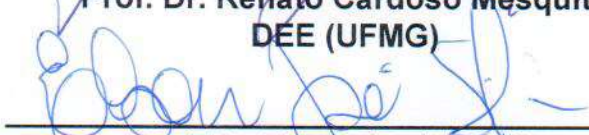
Aprovada em 25 de fevereiro de 2019.
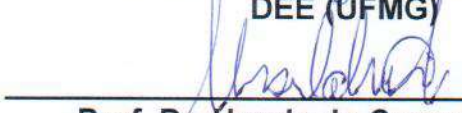
Por:

_____

Prof. Dr. Ricardo Luiz da Silva Adriano
DEE (UFMG) - Orientador

_____

Prof. Dr. Hilton de Oliveira Mota
DEE (UFMG) - Coorientador

_____

Prof. Dr. Renato Cardoso Mesquita
DEE (UFMG)

_____

Prof. Dr. Elson José da Silva
DEE (UFMG)

_____

Prof. Dr. Úrsula do Carmo Resende
DEPTO de Engenharia Elétrica (CEFEC-MG)

_____

Prof. Dr. Adriano Chaves Lisboa
GAIA (GAIA Soluções em Engenharia)

Gratefully dedicated to my beloved Husband Ali for his love and endless efforts in this challenging path and my twin sons Arad and Mehrad who changed my world.

Special thanks from my Parents for their kindness and devotion.

Declaration

I hereby declare that except where specific reference is made to the work of others, the contents of this report are original and have not been submitted in whole or in part for consideration for any other degree or qualification in this, or any other university. This dissertation is my own work and contains nothing which is the outcome of work done in collaboration with others, except as specified in the text and Acknowledgements.

<div align="right">

Naier Mahdinejadgargari
February 2019

</div>

Acknowledgements

First, I am merciful of god, for letting me go successfully through all the steps in my life and giving me strength to do this work.

I would like to express my sincere gratitude to my supervisor Prof. Ricardo Luiz da Silva Adriano, for his patient guidance, encouragements and insightful advices. I have been extremely lucky to have a supervisor who cared so much about my work, and who responded to my questions so promptly. Also, I really appreciate the time he spent helping me and my husband in the early days of our migration to Brazil to take Brazilian documents, registration and housing.

Besides my supervisor, I would like to thank Prof. Hilton de Oliveira Mota, for his great advices and helps during the last year.

Next, I would like to express my special appreciation and thanks to my lovely husband, Ali Moallemi, who has been experiencing all of the ups and downs of my research. His adorable companionship make it easier for me to concentrate on my research career. Also, I would like to thank my twin boys, Mehrad and Arad. They brought more happiness and light to our life.

I would also like to express my gratitude to Vania Silva for her supports. I cannot describe how kind she was and helped me and my husband to be familiar with Brazilian culture and language. We wholeheartedly appreciate everything she had done for us and made us to feel such wonderful days in our first months in Brazil.

Finally, I have to have a special thanks to my dear parents, brothers and specially my sister for all of their encouragements and supports from Iran.

Abstract

Electromagnetic problems at high-frequency are attractive and challenging computational problems to solve. Significant efforts and improvements have been achieved over the last two decades but severe problems remain unsolved. Various numerical approaches have been developed until now such as the Generalized Finite Element Method (GFEM) that is based on the Partition of Unity Method (PUM). GFEM has been proved suitable to solve the two-dimensional Helmholtz equation, where the classical FEM may require a prohibitive mesh refinement. However, when the number of unknowns increases, some difficulties arise, such as bad condition number. Generally, the plane waves configurations in GFEM are chosen to be uniformly distributed. However not all of the wave directions contribute effectively in the solution. Therefore, developing a pre-processing methodology to identify an appropriate number of degrees of freedom for each problem could be useful. The information about the suitable configuration of plane waves for a problem can be obtained using an inaccurate FEM solution generated on a poor resolution mesh (the GFEM mesh). One possibility is to apply the Discrete Fourier Transform (DFT) to extract an acceptable range for the number of wave directions q and effective directions. The simulation results using this methodology is presented in this research and shows that it is capable to choose carefully the wave direction and eliminate some wave directions which has less influence in the solution. Although the mentioned method defines the acceptable range of q for the accurate and converged GFEM solution, it lacks definition of the optimum number of wave directions inside this range. Alternatively, following of the research proposes to use the curvelets transform to achieve local information about wave directions in the domain and therefore identify how many wave directions are necessary to represent the solution accurately. The identified number would be used as the optimum number of wave directions for all nodes in GFEM solution. The results indicate that the adopted strategy can guarantee accurate and converging responses for GFEM in complex problems, along with remarkable reductions of the computational cost as a consequence of reduction in the total number of degrees of freedom.

Resumo

Problemas eletromagnéticos em alta freqüência são problemas computacionais atraentes e desafiadores a serem resolvidos. Embora tenham sido realizado esforços significativos e melhorias ao longo das duas últimas décadas, problemas ainda permanecem sem solução. Várias abordagens numéricas foram desenvolvidas até agora, como o Método de Elementos Finitos Generalizados (GFEM), que é baseado no método de partição de unidade (PUM). O GFEM é adequado para resolver a equação de Helmholtz bidimensional, onde o FEM clássico pode exigir um refinamento de malha proibitivo. No entanto, quando o número de incógnitas aumenta, algumas dificuldades surgem, como o número de condição ruim. Geralmente, as configurações de ondas planas no GFEM são escolhidas para serem uniformemente distribuídas. No entanto, nem todas as direções de onda contribuem eficientemente para a solução. Portanto, o desenvolvimento de uma metodologia de pré-processamento para identificar um número apropriado de graus de liberdade para cada problema poderia ser útil. As informações sobre a configuração adequada das ondas planas para um problema podem ser obtidas usando uma solução FEM imprecisa, gerada em uma malha de baixa resolução (a malha GFEM). Uma possibilidade é aplicar a Transformada Discreta de Fourier (DFT) para extrair um intervalo aceitável para o número de direções de onda q e suas direções efetivas. Esta metodologia é apresentada nesta pesquisa e, embora defina uma faixa aceitável de q para uma solução precisa e convergente, ela não define o número ótimo de direções de onda dentro desta faixa. Alternativamente, esse trabalho também propõe usar a transformada curvelets para obter informações locais sobre as direções de onda no domínio e, portanto, identificar quantas direções de onda são necessárias para representar com precisão a solução. O número identificado seria usado como o número ótimo de direções de onda para todos os nós na solução GFEM. Os resultados indicam que a estratégia adotada pode garantir respostas precisas e convergentes do GFEM em problemas complexos. Outro ponto positivo é a redução do custo computacional como conseqüência da redução número total de graus de liberdade.

Palavras chave_Número de condição, transformada curvilínea discreta rápida, método de elementos finitos generalizados, enriquecimento por ondas planas.

Table of contents

List of figures

List of tables

Nomenclature

Roman Symbols

B magnetic flux density (Wb/m2)

D Electric flux density (C/m2)

E Electric field (V/m)

E_0 Incident Electric Field Amplitude (V/m)

E_a Electric field in domain Ω_a (V/m)

E_b Electric field in domain Ω_b (V/m)

E_i Incident electric Field (V/m)

E_r Reflected Electric Field (V/m)

E_s Scattered Electric Field (V/m)

E_t Transmitted Electric Field (V/m)

H Magnetic field (A/m)

H_i Incident magnetic field (V/m)

H_s Scattered magnetic field (V/m)

J Electric current density (A/m2)

k_0 Wave number in free space

n Normal Vector

r position vector in the Cartesian plane

u arbitrary Vector function

w arbitrary Vector function

Z_0 intrinsic impedance of free space

Greek Symbols

γ a simply closed curve on a complex plane

ι unit imaginary number $\sqrt{-1}$

π $\simeq 3.14\ldots$

Superscripts

j superscript index

Subscripts

0   subscript index

Other Symbols

$\oint_\gamma$ integration around a curve γ

Acronyms / Abbreviations

ABC Absorbing Boundary Conditions

BT Baliss Turkel Conditions

EM Engquist Majda Conditions

$FDCT$ Fast Discrete Curvelet Transform

FDM Finite Difference Method

FFT Fast Fourier Transform

$GFEM$ Generalized Finite Element Method Perfect Matched Layer

MR Multi$_r esolution$

PML Perfect Matched Layer

$USFFT$ Unequally-Spaced Fast Fourier Transform

Chapter 1

Introduction

1.1   Motivation and Background

Computational Electromagnetics (CEM) has become critical in the developments of recent year's technology as the technology shifts to complex microwave and terahertz systems. Accurate and efficient simulations of such systems are very important, especially in the near field, and this depends on the robustness and the accuracy of the computational tools.

The Finite Element Method (FEM) has received much attention in solving electromagnetic problems in the past, because of its flexibility in modeling complex geometries and also the ability to handle complex targets and media [1–3]. In addition, efficient basic finite element solvers were available, which can be parallelized using domain decomposition methods. However, pollution effects in the standard FEM limited its ability for solving large-scale scattering problems and also, when the frequency increases, some difficulties were met [4]. In order to overcome these problems, new finite element methods have been explored such as the Galerkin least squares methods, the element-free methods, the Partition of Unity Method (PUM), and the discontinuous enrichment method [5].

The Generalized Finite Element Method (generalized FEM or GFEM) is also one of the new methods which was originated from the work on the partition of unity method of Babuska and Melenk [6, 7] and also Strouboulis, Zhang, and Babuska [4, 8] for solving coercive elliptic problems (e.g. the Laplace equation, the equation of heat conduction, etc) in problems with complex domains using enrichment by handbook functions. The mathematical aspects of the Generalized Finite Element Methods, including the method proposed here, were addressed in the work of Babuska, Banerjee, and Osborn [9–11] where many more references can be found. It should be mentioned

also, the work on the Extended Finite Element Method (XFEM) by Belytschko et al. [12, 13] which has similar ingredients, and also the work by Duarte et al. [14].

The utilization of wave-related functions to enrich the approximation space for solving the Helmholtz equation was introduced in the Ph.D. thesis of Melenk [6], where the theoretical aspects of the Partition of Unity method for the Helmholtz equation are addressed. Other important works that utilized the plane-wave functions were contributed by Laghrouche, Bettess and co-workers [15], by Ortiz [16], and by Astley and Gamallo [17]. The three-dimensional version of the method was addressed by Perrey-Debain, Laghrouche, et. al. in [18]. There were also related works by Farhat and co-workers [19, 20] on the Discontinuous Enrichment Method (DEM) which also employs enrichment by plane-wave functions using a formulation based on the Discontinuous Galerkin with Lagrange Multipliers, and also the work of Ladev'eze, Rouch, and Riou [21, 22] on the variational theory of complex rays (VTCR) which also uses enrichment of the approximation by local solutions of the wave equation.

The plane wave enrichment reduces the mesh influence allowing solutions with a smaller number of degrees-of-freedom compared with classical FEM. The results presented in [23] point out to an exponential rate of convergence with respect to the number of wave directions q. However, in many cases, increasing the number of directions leads to ill-conditioned systems that makes the GFEM not very attractive for high values of q. The ill-conditioning problem has been reported by many authors. For instance, Laghrouche et al. analyzed the influence of the enrichment functions and the wave number k in the conditioning of the linear system generated by the GFEM [24]. It has been shown that the ill-conditioning increases with the frequency of the problem and grows exponentially as q increases. In [25], a relationship between k and q is proposed in order to keep the condition number within acceptable limits.

This means that for practical problems there is a limit to improve the quality of the solution by increasing the number of plane waves. Moreover, not all the wave directions in uniformly distributed GFEM configuration contribute to the solution of the problem. Furthermore, the development of a pre-processing methodology that is able to avoid the unnecessary wave directions can be very useful to have qualified results.

1.2   Proposed Method

In this work, the Generalized Finite Element Method enriched by Plane Waves is used to solve two-dimensional Helmholtz equation. A systematic approach is proposed to reduce the mesh influence and strongly decrease the number of degrees of freedom of the

final linear system compared with the classical Finite Element Method. The goal is to use the information available during the iterative solution of the linear system to choose carefully the wave direction and eliminate some wave directions which has less influence in the solution. The reduction of the number of wave directions and subsequently reduction of the total number of degrees of freedom, leads to improvements in the condition number of the linear matrix.

The information about the important wave directions in each problem can be achieved using an inaccurate FEM solution generated on a poor resolution mesh (the GFEM mesh). One possibility is to apply the Discrete Fourier Transform (DFT) to this FEM solution and then extract an acceptable range of the number of wave directions q and also the most significant wave directions, using some filtering procedure. Therefore this information could be used to define more efficient configurations for GFEM in comparison to traditional GFEM.

Not all wave directions in the selected configuration are efficient in all parts of the domain. FFT is not capable to define where in the space the most important directions exist. As a result, the same configuration must be used to all parts of the domain. It means that identifying the best number of enrichment functions along with the proper wave directions could improve the GFEM by making the enrichment functions distribution more efficient in the entire domain and decreasing the total number of degrees of freedom. The alternative methodology is to analyze FEM solution data using curvelet transform to identify optimum GFEM configuration. This new configuration with q_{opt} leads to the accurate GFEM solution, besides the smaller number of degrees of freedom, and requires less time and memory in comparison to traditional GFEM. The main objectives of this research can be summarized as follows:

- To propose a systematic approach that is able to determine the suitable range for the number of wave directions for a given problem.

- Identify the optimum number of wave directions in the acceptable range.

- To extract the most important wave directions and determine their respective location in the domain of the problem .

- To suggest the proper enrichment functions distribution for each node in the problem.

- To analyze the pollution and the q-convergence properties of the GFEM to investigate the robustness of the method with respect to problem types.

- Finally, to provide a highly accurate computational GFEM method for the Helmholtz equation on the domain with complex geometries.

1.3   Outlines

Following this introduction, in chapter 2, the mathematical formulation of GFEM enriched by plane wave functions using Cartesian meshes will be briefly described and the main attributes of the Generalized FEM will be also discussed. In chapter 3, the main features of Fast Fourier and Curvelet Transforms as image processing methods will be presented and then the concept of analyzing the FEM solution as an image using these techniques will be introduced. Following that, in chapter 4, the methodology to find out the limits for the number of wave directions and selection of a proper distribution of enrichment functions will be proposed. Simulation results and the cost of the Generalized FEM applying the proposed methodology, will also be analyzed in chapter 4. Finally, the research conclusions and recommendations for the future works are presented in chapter 5.

It should be noted, that the result of this research is as followings:

1. One accepted paper in the $17th$ Biennial Conference on Electromagnetic Field Computation (CEFC 2016). The paper title is "The Condition Number Improvement in a Generalized Finite Element Method Using Discrete Curvelet Transform". This paper was Presented in oral section in CEFC2016 which was held in Miami, USA, 13-16 November, 2016.

2. The extended version of the previous paper was accepted and published in IEEE transactions on Magnetics, 26 January 2017. This paper is related to the proposed methodology of identifying the optimum configuration of enrichment functions for GFEM solution using curvelet transform.

3. Other paper was submitted in The international journal for computation and mathematics in electrical and electronic engineering (COMPEL) in November, 2016. The paper title is "A Pre-Processing Methodology to Identify Wave Directions in the Generalized Finite Element Method" and after the major revision , its status is awaiting for the second review response. This paper is related to the proposed methodology of identifying the acceptable range for number of wave directions using FFT analysis.

Chapter 2

Generalized Finite Element Method Enriched by Plane Waves

During the past two decades meshless computational methods have become increasingly popular with the engineering and science communities. These methods can overcome serious difficulties related to mesh generation for problems involving complicated domains, or on domains whose geometry is solution dependent. They are also utilizable when one wants to incorporate a priori knowledge about the solution of the problem into the design of the computational method. The generalized finite element method (GFEM) is a meshless method that was originated in the work of Babuska et al , and is based on the partition of unity method (PUM) introduced in [4, 1, 7]. It was further analyzed and developed by Strouboulis et al [23, 26].

The main attributes of the GFEM are the capability of using meshes that are independent, or partially independent, of the geometry of the domain and the flexibility in constructing the trial spaces. For high frequency problems, the GFEM can provide accurate results even using less than one point per wavelength. The method is specially interesting for large electromagnetic wave problems where the mesh refinement required by the FEM can become prohibitively expensive [27].

Several mesh free methods proposed in recent years can be formulated as special cases of the partition of unity method. The key feature of these methods is the use of a set of functions whose values sum to the unity at each point in a domain. In these methods, discretization spaces for a Galerkin method are defined using the concept of a partition of unity and local spaces that are built based on a priori knowledge about the solution of a problem.

2.1 GFEM Formulation for Helmholtz Problems

A bounded domain $\Omega \subset R^2$, with boundary $\partial\Omega = \Gamma_1 \cup \Gamma_2, \Gamma_1 \cap \Gamma_2 = \varnothing$ can be seen in Figure 2.1. The field u should satisfy the Helmholtz equation in the following:
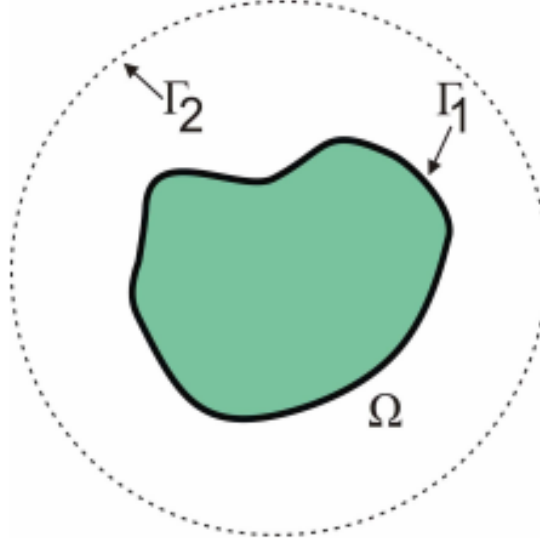
Fig. 2.1 Domain with interior boundary Γ_1 and outer boundary Γ_2

$$-\Delta u - k^2 u = f \quad in \; \Omega \tag{2.1}$$

$$\frac{\partial u}{\partial n_1} = g_1 \quad on \; \Gamma_1 \tag{2.2}$$

$$\frac{\partial u}{\partial n_2} - iku = g_2 \quad on \; \Gamma_2 \tag{2.3}$$

Where k is the wave number, Δ is the laplacian operator, Ω is the studied domain, g_1 and g_2 are the corresponding boundary conditions, i is the imaginary complex number($i^2 = -1$) and the n_1 and n_2 are the outward unit normal to the boundaries Γ_1 and Γ_2 respectively.

2.1.1 Weak Formulation of the Helmholtz Equation

Partial differential equations (PDEs) explained in (2.1), (2.2) and (2.3) are strong-forms of system equations. Obtaining the exact solution for a strong-form of system equation is ideal, but unfortunately it is very difficult for practical engineering problems that are usually complex in nature. The weak-form, in contrast to the strong-form, provides

a variety of ways to formulate methods for approximate solutions for complex systems. Formulation based on weak-forms can usually produce a very stable set of discretized system equations that produces much more accurate results. Applying the weighted residual method, the field $u \in H^1(\Omega)$ should be find such that:

$$\beta(u,v) = \mathcal{L}(v) \quad \forall v \in H^1(\Omega) \tag{2.4}$$

where

$$\beta(u,v) = \int_\Omega \nabla u \, \nabla \bar{v} \, d\Omega - k^2 \int_\Omega u \, \bar{v} \, d\Omega + ik \oint_{\Gamma_2} u \, \bar{v} \, ds \tag{2.5}$$

$$\mathcal{L}(v) = \int_\Omega f \, \bar{v} \, d\Omega + \sum_{i=1}^2 \oint_{\Gamma_i} g_i \, \bar{v} \, ds, \tag{2.6}$$

where $H^1(\Omega)$ is the space of functions with square integrable derivatives over Ω and v is the test function .

2.1.2 Space of GFEM: Partition of Unity

For solving the Helmholtz equation, GFEM can be obtained by employing the traditional FEM method and by enriching the approximation by plane waves pasted into the finite element basis at each mesh node using the partition of unity method [28, 26, 23]. This means that, the space of Generalized Finite Element solutions can be constructed by combining the following discrete spaces of functions on the mesh Δ_h

1. The standard bi-p (tensor product) finite element space, $S^p_{\Delta_h}$ (p is related to the degree of the polynomial functions.)

2. The partition of unity space:

$$W^{k;q}_{\Delta_h} = \left\{ v = \sum_{i=1}^{nnodes} \phi_i^{\Delta_h} \, v_i \quad | \quad v_i \in W^{k;q}_{loc}(\omega_i^{\Delta_h}) \right\} \tag{2.7}$$

where

$$W^{k;q}_{loc} = span\left\{ w_k = exp\left(ik \left(x\cos\frac{2\pi l}{q} + y\sin\frac{2\pi l}{q} \right) \right), l = 0, ..., q-1 \right\}. \tag{2.8}$$

is the local space of linear combinations of plane waves traveling in the directions $(\cos\frac{2\pi l}{q}, \sin\frac{2\pi l}{q})$

2.1.3   GFEM Shape Function

A shape function, φ_{il}, in the GFEM is computed from the product of a linear finite element shape function, ϕ_i , and an enrichment function, Ψ_{il}.

$$\varphi_{il}(x) = \phi_i(x)\,\Psi_{il}(x) \tag{2.9}$$

where i is a node in the finite element mesh. As mentioned previously, the linear finite element shape functions ϕ_i , $i = 1, ..., n$, in a finite element mesh with n nodes constitute a partition of unity, as stated by the following equation for all x in a domain Ω covered by the finite element mesh.

$$\sum_{i=1}^{n} \phi_i(x) = 1,\ \forall x \in \Omega \tag{2.10}$$

(a)   (b)
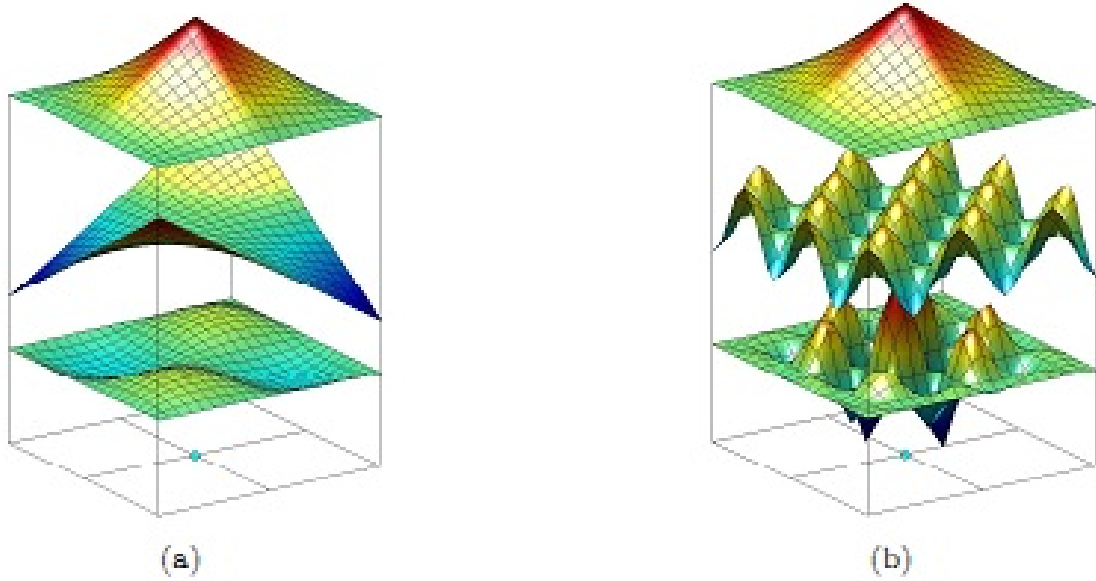
Fig. 2.2 Construction of a Generalized FEM shape function using a (a) polynomial (b) and a non-polynomial enrichment Functions [29].

Figure 2.2, illustrates the construction of GFEM shape functions. Here, ϕ_i are the functions at the top, the enrichment functions, Ψ_{il} , are the functions in the middle, and the generalized FE shape functions, φ_{il} , are the resulting bottom functions. This is a key property used in the partition of unity methods. Linear combinations of the GFEM shape functions φ_{il} , $i = 1, ..., n$, can represent exactly any enrichment function Ψ_{il} [30, 31].

2.1.4   GFEM Solution

The GFEM approximation for the solution is constructed using the FEM nodal shape functions and a set of plane waves and can be expressed as :

$$u(x) = \sum_{i=1}^{n} N_i(x)\beta_i + \sum_{i=1}^{n}\sum_{l=1}^{q} \phi_i(x)\Psi_{il}(x)\alpha_{il} = u^{FEM}(x) + u^{enr}(x) \qquad (2.11)$$

where β_i and α_{il} are the degrees-of-freedom and $N_i, i = 1, ..., n$ is the i-th first order Lagrange basis function. When the functions $\phi_i(x)$ have compact support, then the discrete equations for the system will be sparse. In general $\phi_i(x) = N_i(x)$. In this case the expression in (2.11) could be written in the matricial form as:

$$u(x) = \boldsymbol{\Phi^T}.\boldsymbol{U} \qquad (2.12)$$

where

$$U^T = [\beta_1 \quad \alpha_{11} \quad ... \quad \alpha_{1q} \quad ... \quad \beta_n \quad \alpha_{n1} \quad ... \quad \alpha_{nq}] \qquad (2.13)$$

and

$$\Phi^T = [N_1 \quad N_1\Psi_{11} \quad ... \quad N_1\Psi_{1q} \quad ... \quad N_n \quad N_n\Psi_{n1} \quad ... \quad N_n\Psi_{nq}] \qquad (2.14)$$

2.1.5   Plane Wave Enrichment Function

In (2.11), the $\Psi_{il}, l = 1, ..., q$, is the enrichment function given by

$$\Psi_{il}(\boldsymbol{r}) = \exp\left(jk\boldsymbol{\xi}_l \cdot \boldsymbol{r}\right) \qquad (2.15)$$

where $\boldsymbol{r}$ is the position vector of a considered point, $j = \sqrt{-1}$ and k is the wave number. Generally, the wave functions in the traditional GFEM are chosen to be uniformly distributed. This is done because the information about the behavior of the electromagnetic fields is rarely available a priori. Mathematically, the wave directions can be described as:

$$\boldsymbol{\xi}_l = cos(\theta_l)\hat{x} + sin(\theta_l)\hat{y}, \qquad (2.16)$$

where $\theta_l = \frac{2\pi l}{q}$, $l = 0, ..., q - 1$.

Figure 2.3 depicts the employed wave directions for q = 1,...,6, in uniformly distributed configuration. As shown in [24], not all of these wave directions contribute to the solution.
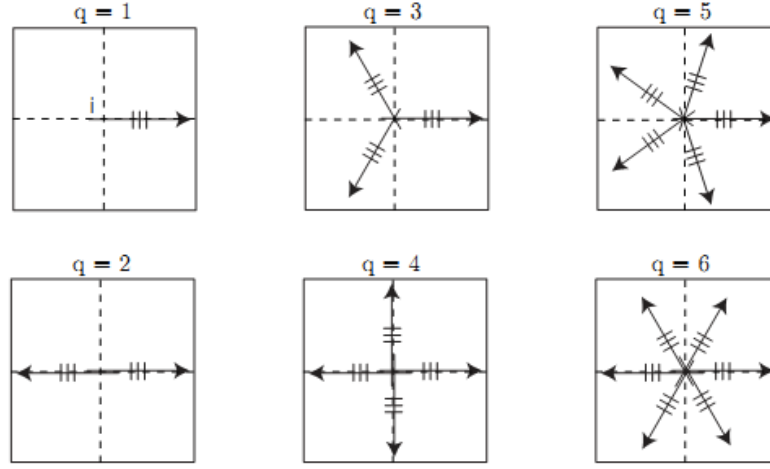
Fig. 2.3 Example of wave directions in equally spaced distribution to construct the enrichment Functions

In a matricial form, the unknown function in GFEM solution in expressions (2.11), would be written as :

$$u = \sum_{i=1}^{n}\sum_{l=1}^{q} N_i \Psi_{il}\alpha_{il} = \boldsymbol{P}.\boldsymbol{A} \tag{2.17}$$

where vector $\boldsymbol{P}$ contains the oscillatory shape functions which are products of polynomials and planar waves and the $\boldsymbol{A}$ is the vector of the unknown amplitudes. A Galerkin scheme is used so that the weighting functions are chosen to be the same as the interpolating oscillatory functions. The set of Galerkin equations of expressions (2.4), (2.5) and (2.6) may be written in a matricial form :

$$\boldsymbol{K}.\boldsymbol{A} = \boldsymbol{f} \tag{2.18}$$

where

$$\boldsymbol{K} = \int_{\Omega}\left(\triangledown\boldsymbol{P}^T\triangledown\boldsymbol{P} - k^2\boldsymbol{P}^T\boldsymbol{P}\right)d\Omega + jk\int_{\Gamma}\boldsymbol{P}^T\boldsymbol{P}d\Gamma \tag{2.19}$$

and

$$\boldsymbol{f} = \sum_{i=1}^{2}\int_{\Gamma}\boldsymbol{P}^T g_i d\Gamma \tag{2.20}$$

For coarse meshes, the first term of the right-hand side of (2.11) introduces high numerical dispersion with a poor capacity to deal with the oscillatory nature of the function, and therefore, it is discarded by several authors [32]. As a result, the β_i in (2.11) is supposed to be zero for $i = 1,...,n$ in this research and then the dimension of the resulting system of equations would be equal to $nq \times nq$. The global system

matrix $\boldsymbol{K}$ is the contribution of the local matrices of total elements in the domain and boundaries. In this research the triangular elements are used to discretize inside the domain and line elements are used for boundaries. Therefore $\boldsymbol{K_e}$ by the size $3q \times 3q$ is calculated for each element and then substituted to the respective location in $\boldsymbol{K}$. In addition, the $\boldsymbol{K_s}$ in size $2q \times 2q$ and also f in size $2q \times 1$ are calculated for line elements on the boundaries. The position of each element in the global system is defined by transferring local node numbers to global ones.

2.1.6   Numerical Integration

The integration for $\boldsymbol{K_e}$ should be performed over the whole element. However, there is not always feasible analytical expressions for P or equally for Ψ. The solution is to use the numerical integration to approximate the integration over the element; The Gauss quadrature method that is a weighted sum of function values at specified points within the domain of integration is usually used in FEM problems for approximation.

$$\boldsymbol{K_e} = \int_{\Omega_e} \left(\triangledown \boldsymbol{P}^T \triangledown \boldsymbol{P} - k^2 \boldsymbol{P}^T \boldsymbol{P} \right) d\Omega_e = \int \int_{xy} F(x,y)\, dxdy \qquad (2.21)$$

To evaluate the Integral in (2.21) by Gaussian quadrature rule, first the triangular element Ω_e should be transformed to the standard triangular element T_{st} as shown in Fig.2.4.
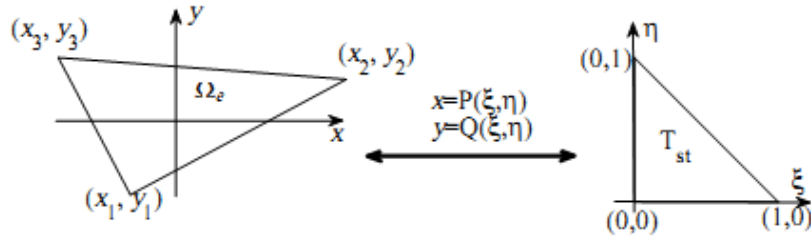
Fig. 2.4 Linear mapping between triangular element and standard triangle

The nodal shape functions in the standard triangle are expressed as follows:

$$N_1(\xi,\eta) = \xi$$
$$N_2(\xi,\eta) = \eta \qquad (2.22)$$
$$N_3(\xi,\eta) = 1 - \xi - \eta$$

The mapping can be achieved conveniently by using the nodal shape functions as follows:

$$x = P(\xi,\eta) = \sum_{i=1}^{3} x_i N_i(\xi,\eta) = x_1 N_1(\xi,\eta) + x_2 N_2(\xi,\eta) + x_3 N_3(\xi,\eta) \qquad (2.23)$$

$$y = Q(\xi,\eta) = \sum_{i=1}^{3} y_i N_i(\xi,\eta) = y_1 N_1(\xi,\eta) + y_2 N_2(\xi,\eta) + y_3 N_3(\xi,\eta) \qquad (2.24)$$

Then

$$\int\int_K F(x,y)dxdy = \int\int_{T_{st}} F(P(\xi,\eta),Q(\xi,\eta))|J(\xi,\eta)|d\xi d\eta \qquad (2.25)$$

where $J(\xi,\eta)$ is the Jacobian of the transformation, namely,

$$J(\xi,\eta) = \left|\frac{\partial(x,y)}{\partial(\xi,\eta)}\right| = \begin{vmatrix} \frac{\partial x}{\partial \xi} & \frac{\partial y}{\partial \xi} \\ \frac{\partial x}{\partial \eta} & \frac{\partial x}{\partial \eta} \end{vmatrix} = 2A_K \qquad (2.26)$$

Here A_K represents the area of the triangle Ω_e, which can be evaluated by:

$$A_K = \frac{|x_1(y_2 - y_3) + x_2(y_3 - y_1) + x_3(y_1 - y_2)|}{2} \qquad (2.27)$$

The inverse of the transformation shown in Fig.2.4 can be found as:

$$\xi = \frac{1}{2A_K}[(y_3 - y_1)(x - x_1) - (x_3 - x_1)(y - y_1)] \qquad (2.28)$$

$$\eta = \frac{1}{2A_K}[-(y_2 - y_1)(x - x_1) + (x_2 - x_1)(y - y_1)] \qquad (2.29)$$

Finally, by applying the Gaussian quadrature of degree N_g (number of Gauss points) for the standard triangular element, (2.25) yields:

$$\int\int_K F(x,y)dxdy \approx A_k \sum_{i=1}^{N_g} w_i\, F(P(\xi_i,\eta_i),Q(\xi_i,\eta_i)) \qquad (2.30)$$

Here N_g is the number of Gauss points and w_i is the weight for each Gauss point. Position of sampling points and value of weights were both optimized. Now it is possible to calculate (2.21) using (2.30).

For calculating the integral in (2.21), the vector $\boldsymbol{P}$ should be defined in triangle which is expressed previously in (2.17). where vector $\boldsymbol{P}$ contains the oscillatory shape functions which are products of polynomials and planar waves and the $\boldsymbol{A}$ is the vector

of the unknowns amplitudes as follows:

$$P_e = \sum_{i=1}^{3} \sum_{l=1}^{q} P_{il} = \sum_{i=1}^{3} \sum_{l=1}^{q} N_i \Psi_{il} \tag{2.31}$$

$$A_e^T = [\alpha_{11} \quad ... \quad \alpha_{1q} \quad ... \quad \alpha_{31} \quad ... \quad \alpha_{3q}] \tag{2.32}$$

and

$$P_e = [N_1 \Psi_{11} \quad ... \quad N_1 \Psi_{1q} \quad ... \quad N_3 \Psi_{31} \quad ... \quad N_3 \Psi_{3q}] \tag{2.33}$$

Considering the expression of $\boldsymbol{P}$, the ∇P_{il} would be equal to :

$$\nabla P_{il} = \begin{bmatrix} \frac{\partial P_{il}}{\partial x} \\ \frac{\partial P_{il}}{\partial y} \end{bmatrix} = \left\{ \begin{bmatrix} \frac{\partial N_i}{\partial x} \\ \frac{\partial N_i}{\partial y} \end{bmatrix} + jkN_i \begin{bmatrix} \cos\theta_l \\ \sin\theta_l \end{bmatrix} \right\} \Psi_{il} \tag{2.34}$$

The derivative of shape functions N would be substituted by B matrix :

$$B = \begin{bmatrix} \frac{\partial N_1}{\partial x} & \frac{\partial N_2}{\partial x} & \frac{\partial N_3}{\partial x} \\ \frac{\partial N_1}{\partial y} & \frac{\partial N_2}{\partial y} & \frac{\partial N_3}{\partial y} \end{bmatrix} \tag{2.35}$$

According to (2.22) and (2.28), the derivatives could be calculated by:

$$\frac{\partial N_i}{\partial x} = \frac{\partial N_i}{\partial \xi} \cdot \frac{\partial \xi}{\partial x} \tag{2.36}$$

$$\frac{\partial N_i}{\partial y} = \frac{\partial N_i}{\partial \eta} \cdot \frac{\partial \eta}{\partial y} \tag{2.37}$$

In which

$$\frac{\partial N}{\partial \xi} = \begin{bmatrix} 1 & 0 & -1 \end{bmatrix} \tag{2.38}$$

$$\frac{\partial N}{\partial \eta} = \begin{bmatrix} 0 & 1 & -1 \end{bmatrix} \tag{2.39}$$

2.2   Influence of Wave Directions on GFEM Solution

As shown in [24], not all of the wave directions in (2.16) contribute to the solution. The free space problem is used as an example to illustrate the influence of the wave directions in GFEM solution with equally distributed configuration. This problem consists of a square domain $\Omega = \{(x,y), |-3 \le x \le 3|, |-1.5 \le y \le 1.5|\}$, with the wave number set as $k = 2\pi$. Fig.2.5 shows the discretized domain with mesh size $h = 1.1\lambda$.
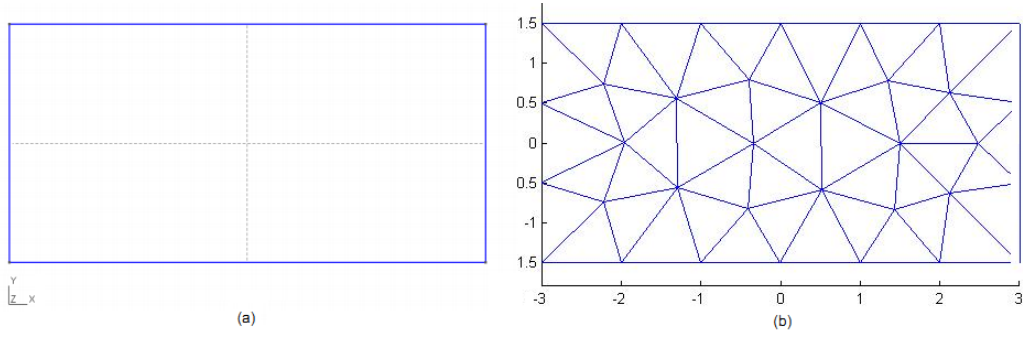
Fig. 2.5 a)free space geometry, b) Domain discretization, mesh size $h = 1.1\lambda$

The problem is solved considering an incident plane wave with an angle of incidence $\theta_i = 15^o$ propagating in the free space domain. As the analytical solution of this problem has only one wave direction, it is expected that the wave directions which are aligned with the analytical one contribute more significantly to represent the solution. Fig. 2.6 illustrates the solution of the problem with a mesh size $h = 1.1\lambda$ and $q = 18$. It shows the plane wave magnitude values α_{il} obtained in two nodes of the mesh. As it can be seen, the directions closest to the incident one, $l = 0$ and $l = 1$ (corresponding to $\theta = 0^o$ and $\theta = 20^o$), contribute more significantly to the solution.
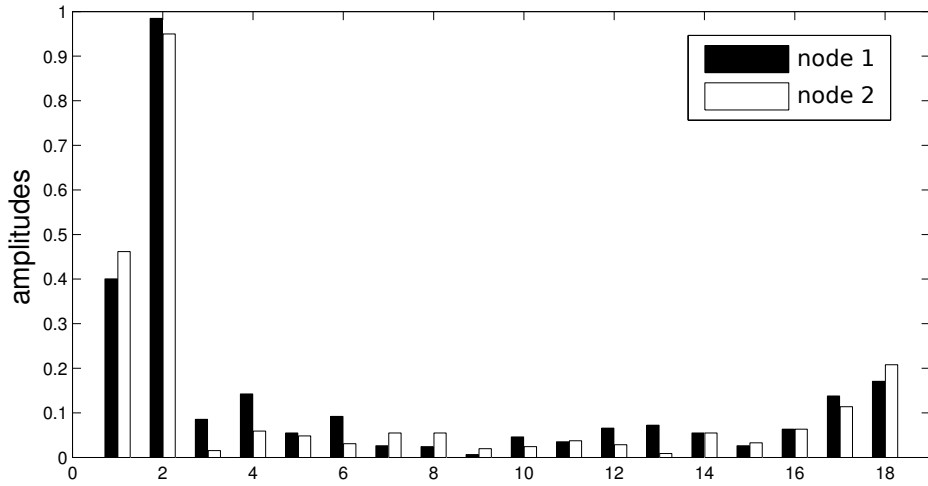
Fig. 2.6 Wave amplitudes at two different nodes of the mesh.

2.3   q-convergence of GFEM

To analyze the convergence of the GFEM, the accuracy of the model is measured by the relative $L^2(\Omega)$ error defined in the whole computational domain as following:

$$\epsilon = \frac{\left\|u_{ref} - u_{num}\right\|_{L^2(\Omega)}}{\left\|u_{ref}\right\|_{L^2(\Omega)}} \tag{2.40}$$

where reference result is a vector containing the analytical field value at the nodes of the mesh and numerical result is generated from GFEM solution. The error due to evaluation of $\boldsymbol{K}$ and $\boldsymbol{F}$ by numerical integration is negligible.

The GFEM solution for the free space problem with 34 nodes and $\theta_i = 15^o$ is calculated by employing the 7×7 Gauss-Legendre integration rule in the triangle elements inside the domain, while 7 Gauss= points was applied for the line elements on the boundaries. The error value versus the number of wave directions is shown in Fig. 2.7. As can be seen the error decreases by increasing the number of wave directions until $q = 16$. It means that the GFEM solution has converged exponentially to the analytical solution and meet the best convergence at $q = 16$. However, increment in the error can be seen when $q > 16$ as side effect of increment in the condition number. Basically, when the number of wave directions increases the difference between the directions decreases and then the global matrix would be ill-conditioned.

As mentioned in q-convergence property of the GFEM solution, it is important to choose a suitable q for the calculations which leads to converged solution. On the other hand, as mentioned in previous section not all of the wave directions in uniformity distributed plane wave directions have influence in the accurate solution. Therefore applying a systematic approach to choose carefully the number and also the important wave directions for each problem, could result in convergence and accurate solutions with smaller computational cost. The next chapter is dedicated to explanation of extracting the appropriate plane wave configuration using image processing techniques.
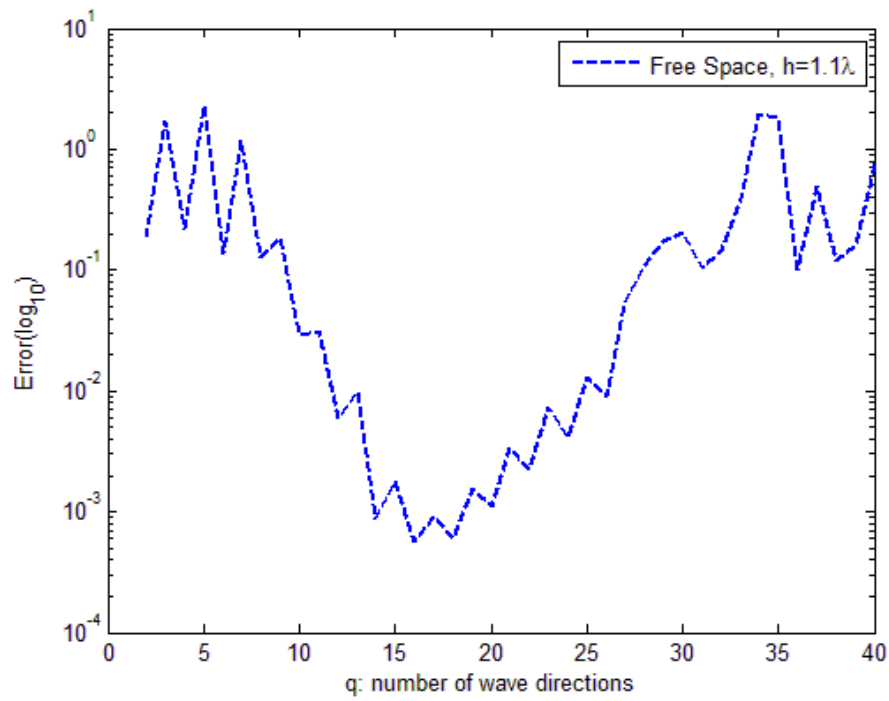
Fig. 2.7 q-convergence of GFEM in free space problem with $k = 2\pi$ and $h = 1.1\lambda$.

Chapter 3

Identifying Important Plane Waves Directions

In GFEM formulation, the field value at each finite element node is expanded in discrete series of plane waves, each propagating at a specified angle. Generally, these angles are uniformly distributed and are the same for all nodes of the mesh. Such systems of plane waves form complete sets of functions for the Helmholtz equation. However, as described in section 2.2, the distribution of the amplitudes with respect to the directions of the basis functions showed that only a few directions are active. This means that the directions should be chosen carefully and may vary from one node to another in the studied mesh.

On the other hand, the conditioning of the plane wave approximation of finite element model for the Helmholtz equation was analyzed (by Laghrouche et al) when the number of the planar waves are increased [15]. It appears that conditioning for problems grows exponentially when the number of the approximating plane waves increases [24]. Therefore, it is valuable to take reasonable numbers of basic functions and even reduce this number at nodes of the problem where the directions of propagation are approximately known to avoid ill-conditioning solutions.

As a consequence, developing a pre processing methodology to choose the Number of the approximating plane waves and also the active directions could be advantageous to have smaller number of degrees of freedom. The fact behind the proposed idea in this research is that the FEM solution of the problem can be seen as an image. Therefore, the image processing tools has been used to analyze the FEM solution image of each problem. Feature extraction capabilities of two image processing methods, Fast Fourier Transform (FFT) and Fast Discrete Curvelet Transform(FDCT) are discussed

in this chapter. These transforms has been used in the proposed methodologies in this research to extract the appropriate plane waves distribution for GFEM solution.

3.1   Feature Extraction Using Discrete Fourier Transform (DFT)

The Fourier Transform is an important image processing tool which is used to decompose an image into its sine and cosine components. The output of the transformation represents the image in the Fourier or frequency domain, while the input image (in this research, the solution of the wave equation) is the spatial domain equivalent. In the Fourier domain image, each point represents a particular frequency contained in the spatial domain image. The DFT is the sampled Fourier Transform and therefore does not contain all frequencies forming an image, but only a set of samples which is large enough to fully describe the spatial domain image. The number of frequencies corresponds to the number of pixels in the spatial domain image, i.e. the image in the spatial and Fourier domain are of the same size.

The proposed idea in this research is to apply the Discrete Fourier Transform (DFT) to perform the Spatial Fourier Transform (SFT) on the coarse-mesh finite element solution to extract useful information a priori about wave directions in GFEM configuration. It should be noted that the appropriate size for the FEM mesh (also used as the GFEM mesh) is selected considering the Nyquist sampling theory (3.1).

$$\text{Sampling frequency limit}: f_s > 2.f_{max} \tag{3.1}$$

In which f_s is the sample rate per unit of space and f_{max} is the highest frequency component of interest in the measured signal [33]. The maximum spatial frequency and the minimum wavelength of the propagating wave are related subsequently by (3.2). Therefore the acceptable coarse mesh size is defined. It should be smaller than the half of the minimum existent wavelength.

$$k = 2\pi/\lambda \tag{3.2}$$

Since the input form of DFT should be equally-spaced samples, the FEM solution is evaluated over a grid with M equally spaced points along the x axis and N equally spaced points along the y axis. Once the $M \times N$ Matrix is constructed, it is possible to visualize the wave components of the FEM solutions as a two-dimensional image by employing the DFT. The image can be created using the information of the entire

domain or some region of interest. The Discrete Fourier Transform formulation gives the wave number spectrum along both axis as follows [33]:

$$F(U,V) = \sum_{m=1}^{M} \sum_{n=1}^{N} f(m,n) exp[-j2\pi(Um/M + Vn/N)] \qquad (3.3)$$

where $2\pi U$ is the wave number component along the x direction, $2\pi V$ is the wave number component along the y direction and $f(m,n)$ is the finite element solution on the point with (m,n) coordinates.

3.1.1 A Proposal to Find the Most Important Wave Directions Applying DFT

The free space problem is used as an example to illustrate the capability of DFT on identifying the extant wave directions on image of FEM solution. This problem consists of a square domain $\Omega = \{(x,y), |-3 \leq x \leq 3|, |-1.5 \leq y \leq 1.5|\}$, with the wave number set as $k = 2\pi$ ($\lambda = 1m$). Different discretizations are used to solve the problem. Fig. 3.1 shows the discretized domains obtained using two meshes: the first one composed of 109 nodes (2.5 nodal points per wavelength) and the second one composed of 633 nodes (5.0 nodal points per wavelength).
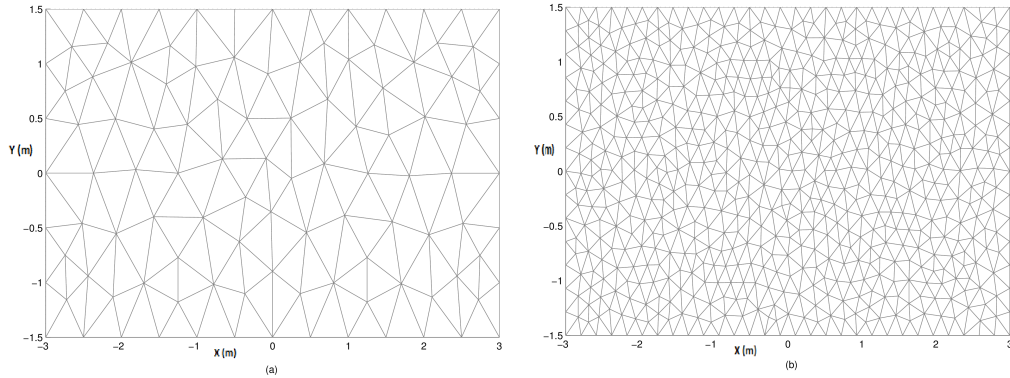
Fig. 3.1 Domain discretization a) mesh size $h = 0.4\lambda$ and b) mesh size $h = 0.2\lambda$

The problem was solved considering a sum of two incident plane waves with angles of incidence $\theta_1 = 15^o$ and $\theta_2 = 80^o$. The image of FEM solution with h=0.2λ can be seen in Fig. 3.2. Applying the DFT, the wave number spectrum of a finite element solution can be represented as an image, as shown in Fig. 3.3. It is easy to see that more noise is introduced into the solution as the mesh size approaches the Nyquist rate.
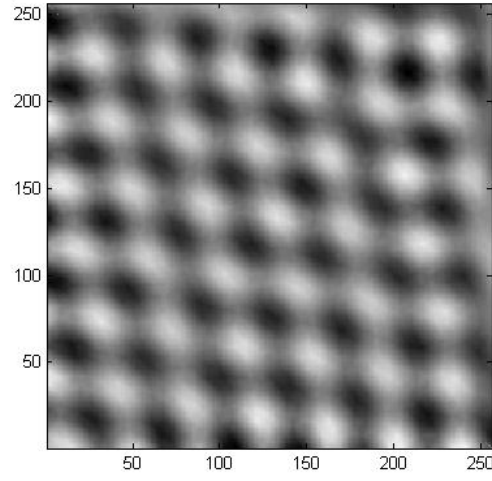
Fig. 3.2 Image of FEM solution with two incident angles
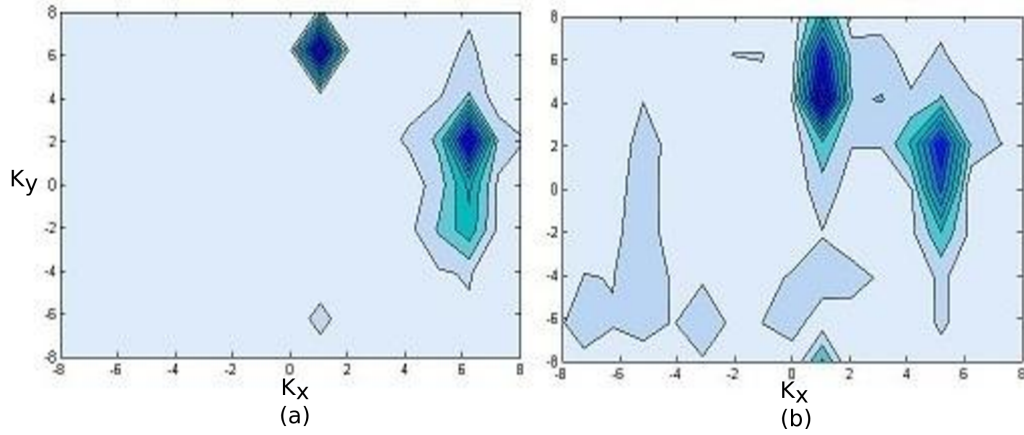
Fig. 3.3 2-D DFT of the finite element solution a) $h = 0.2\lambda$, b) $h = 0.4\lambda$

With this spectrum, the significant plane waves directions can be easily obtained by calculating the angles where the peaks occur. To simplify the problem and to offer better results, a radial spatial mask is used to select only the values within a radius from the center of the spectrum. Since a time harmonic solution is expected, the radius is set to match the wave number of the problem.

The filtering procedure reduces the problem to a 1-D peak detection problem, as presented in Fig. 3.4. In both meshes, the two main peaks occur when θ is approximately $15°$ and $80°$, matching the incidence angles assigned in the testing problem. Other remaining peaks exist, especially when $h = 0.4\lambda$. However, the amplitude of those peaks are considerable smaller than the main ones. They can be eliminated using a cut-off value based on the amplitude of the highest peak.
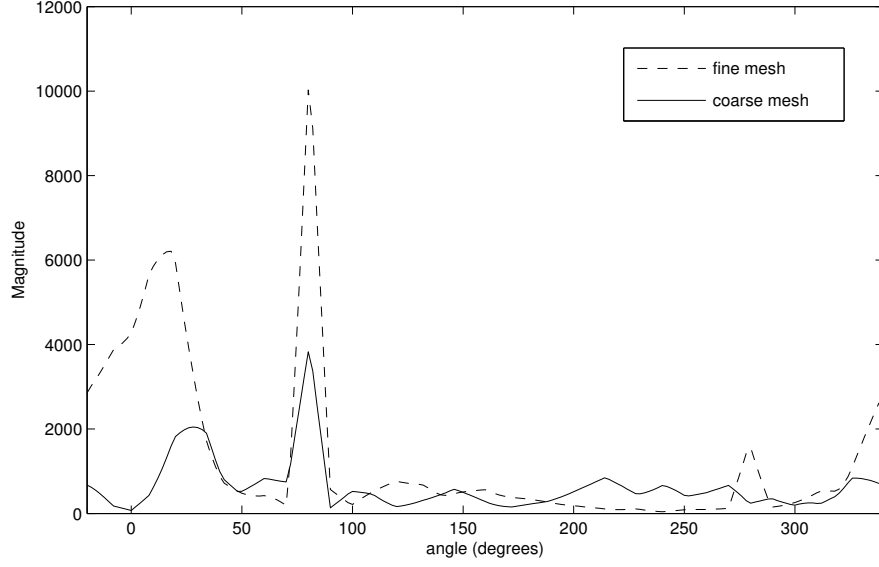
Fig. 3.4 1-D problem obtained after the filtering process. Meshes $h = 0.2\lambda$, $h = 0.4\lambda$

3.1.2   Find Multiple Incident Wave Directions in Free Space Problem

Using the filtering procedure, the method is capable of identifying the multiple important wave directions which composes the solution with good precision. Table 3.1 shows the wave directions identified for seven different configurations of incident waves. In this table, θ_i represents the directions of the incident waves imposed to the problem and θ_f represents waves identified by the DFT. The cut-off value was chosen as 0.5 of the amplitude of the main direction.

Table 3.1 Wave directions identified using the 0.2λ mesh

Configuration	θ_i (degrees)	θ_f (degrees)
1	[15 140]	[18 140]
2	[50 130]	[48 132]
3	[70 230]	[70 132 228 290]
4	[42 150 244]	[42 120 146 240]
5	[15 75 160]	[8 78 162]
6	[30 120 230 320]	[34 228 314]
7	[40 70 155 245]	[40 70 118 160]

The wave directions identified by the DFT show a good agreement with the incident ones. Except by one direction in configuration 6, all incident waves were identified properly. The standard deviation between θ_i and θ_f is about 2.12^o. Nevertheless, some wave directions that do not correspond to an incident one were introduced in

the θ_f vector. This phenomena can be observed in configurations 3 and 4 and it is a consequence of the choice of the cut-off parameter.

Table 3.2 shows the results obtained using the 0.4λ mesh. In this case, the noise introduced by the low quality mesh made the identification much more sensitive to the cutoff parameter and more undesired directions were selected. Even though, only two wave directions were not found (see row 5 of the table) and the standard deviation between θ_i and θ_f is about 5.89^o. Fortunately, as will be shown in the next sections, the number of identified angles is used only to estimate the lower limit for the range of suitable choices of q. As a consequence, the overall method is quite insensitive to the cut-off parameter.

Table 3.2 Wave directions identified using the 0.4λ mesh

Configuration	θ_i (degrees)	θ_f (degrees)
1	[15 140]	[22 48 132 148 218]
2	[50 130]	[48 132]
3	[70 230]	[70 132 228 290 310]
4	[42 150 244]	[48 120 152 240]
5	[15 75 160]	[80]
6	[30 120 230 320]	[26 48 130 240 312]
7	[40 70 155 245]	[48 70 120 152 280]

3.2 Feature Extraction Using the Discrete Curvelet Transform (DCT)

The most important directions in the wave propagation problems can be defined by applying FFT analysis on the Coarse mesh FEM solution of the problem. However, the FFT is not able to define where in the space the most important directions exist. It means that, using the Fourier Transform the FEM data is being transformed into waves with specific frequencies and directions that are supposed to exist in the whole space domain. To overcome this resolution problem a multiresolution transform is used to transform the FEM data which is known as the Curvelet Transform. Curvelets are useful because they are limited in space and frequency. Details of the theory of curvelet transform and its ability to identify the most important directions in different parts of the problem are described in the following sections.

3.2.1   The Curvelet Transform

Motivated by the need of image analysis, Candes and Donoho developed the curvelet transform in 2000 [34]. The curvelet transform is a highly redundant dictionary which can provide sparse representations of signals that have edges along regular curves. The initial construction of curvelet was redesigned later [35] and was re-introduced as a Fast Discrete Curvelet Transform (FDCT) [36]. This second generation of curvelet transform is meant to be simpler to understand and use. It is also faster and less redundant compared to its first generation version. Curvelet transform is defined in both continuous and digital domain and for higher dimensions.

A single curvelet is function that obey the paramount parabolic scaling principle: $width = length^2$, in space and frequency domain as can be seen in Fig. 3.5. By translating the curvelet function, the whole 2D space would be covered. In addition, different frequencies and orientations are covered by expanding and rotating the curvelet. By doing all simultaneously, the curvelet transform covers the whole frequency spectrum so that there is no loss of information. This means that Curvelets represent a family of functions formed from translations, rotations, and parabolic scaling of a "mother" wave.
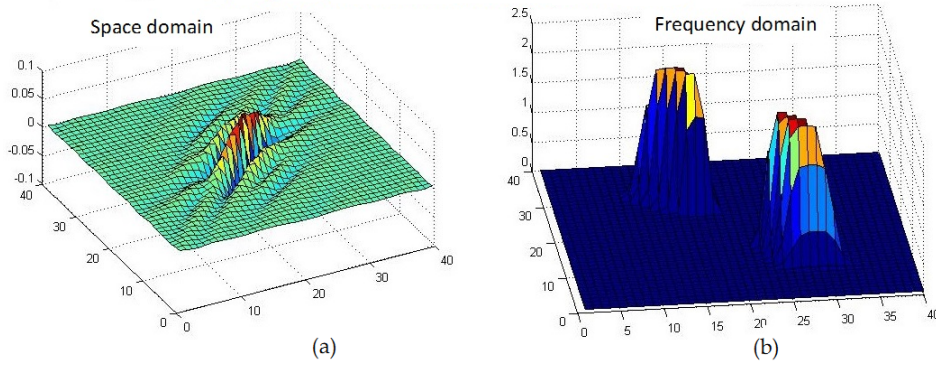
Fig. 3.5 A single curvelet in a) space domain and b) frequency domain

In order to implement the curvelet transform, first the 2D Fast Fourier Transform (FFT) of the image and a curvelet function is taken. Then the convolution of the curvelet with the image in spatial domain becomes the product in Fourier domain. Finally, the curvelet coefficients are obtained by applying the inverse Fourier transform on the spectral product. As shown in Fig. 3.6 (a), the 2D Fourier frequency plane is divided into wedges. The parabolic shape of wedges is the result of partitioning the Fourier plane into radial (concentric circles) and angular divisions. The concentric circles are responsible for the decomposition of an image into multiple scales (used for

band passing the image at different scale) and the angular divisions partition the band passed image into different angles or orientations. Each of the wedges corresponds to a particular curvelet (shown as ellipses) at a given scale j and angle l. This indicates that if the inverse FFT of a particular wedge is taken, it will determine the curvelet wave for that scale and angle. This is the main idea behind the implementation of curvelet transform. Fig. 3.6 (b) represents the support of curvelet in spatial Cartesian grid associated with a given scale and angle.
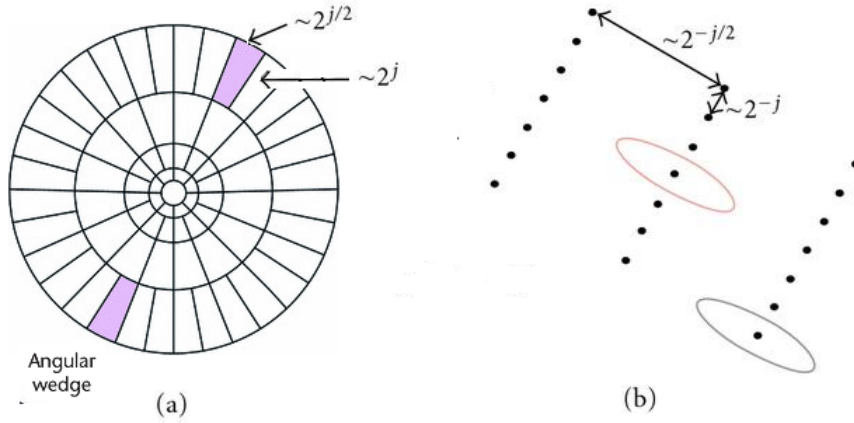
Fig. 3.6 Curvelet tiling of space and frequency. a) The induced tiling of the frequency plane and b) The spatial Cartesian grid associated with a given scale and orientation

Curvelets are local in both space and spatial frequency. Fig. 3.7 represents six different curvelets in frequency and spatial domain at different scales and directions. As can be seen, the main axes in the frequency domain and the space domain are orthogonal to each other in the curvelet transform. As opposed to complex curvelets, real curvelets live in two angular wedges symmetric about the origin. As such, curvelets form a frame with moderate redundancy.

3.2.2 Curvelet Comparison to Wavelet

Curvelets were developed to overcome inherent limitations of traditional multistage representations such as wavelet and Gabor transforms [35]. Although, wavelets are widely used in image processing, but it failed to handle randomly oriented edges of the object and the singularities of the object. Gabor filters overcome the limitation of the wavelet transform and deal with the oriented edges, it loses the spectral information of the image. Curvelet transform is used to overcome these problems of the wavelet and Gabor filters.
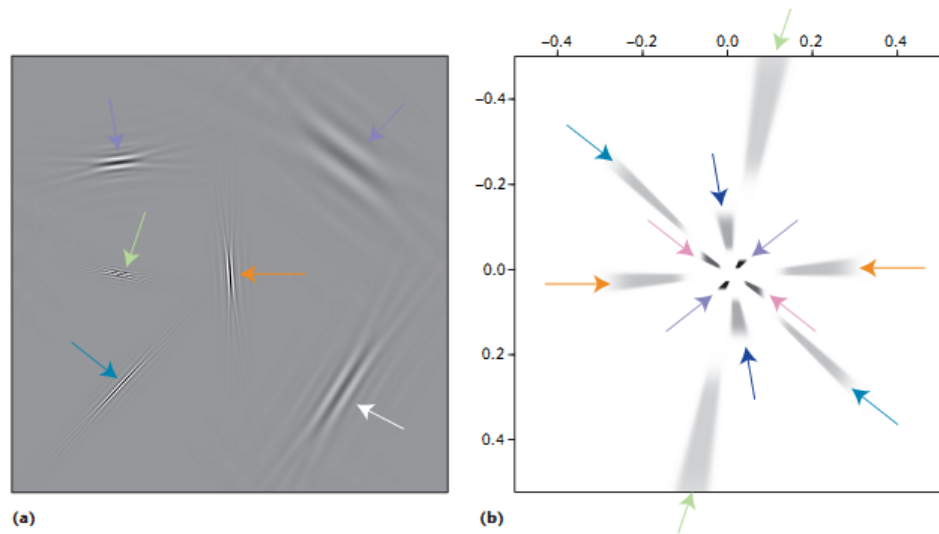
Fig. 3.7 Viewpoints of six real curvelets at different scales and angles in a) Spatial and b) Frequency domain

The main idea is that the edge discontinuity is better approximated by curvelets rather than wavelets. Curvelets can provide solutions for the limitations (curved singularity representation, limited orientation and absence of an-isotropic element) that the wavelet transform suffer from, as shown in Fig. 3.8. More wavelets are required for an edge representation using the square shape of wavelets at each scale, compared to the number of required curvelets. Actually, the needle-shape elements of this transform have very high directional sensitivity and anisotropy. It can be considered as a higher dimensional generalization of wavelets which have the unique mathematical property to represent curved singularities effectively in a non-adaptive manner.
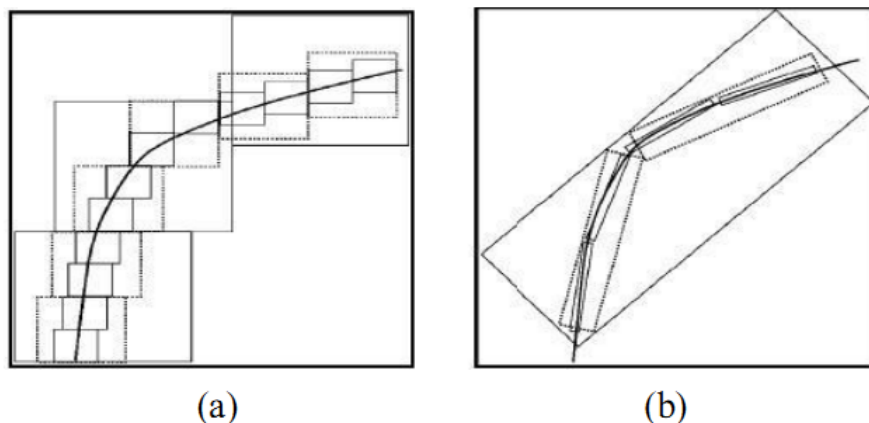
Fig. 3.8 Representation of curved singularities using a) Wavelet and b) Curvelet [37]

What makes the curvelet appropriate for processing wave propagation data is its capability to obtain the complete spectral information of the image while dealing with the different local orientations of the image edges.

3.2.3   Applications of Curvelet Transform

Curvelet transform is gaining popularity in different research areas, like signal processing, image analysis and seismic imaging. It has been successfully used as an effective tool in image denoising [38], image decomposition [39], image deconvolution, astronomical imaging, contrast enhancement [40] and etc.

Recently, curvelets have also been employed to address several pattern recognition problems, such as face recognition [41], optical character recognition [42] and finger-vein pattern recognition [43]. One example of image denoising using curvelet and wavelet is presented in Fig. 3.9. It is suggested to go through the referred works for further information on various applications of the curvelet transform.

3.2.4   Fast Discrete Curvelet Transform

There are two different digital implementations of FDCT:

1. Curvelets via USFFT (Unequally Spaced Fast Fourier Transform)

2. Curvelets via Wrapping

Both variants are linear and take a Cartesian array as input to provide an output of discrete coefficients indexed by scale, orientation and location parameters. The two implementations only differ in choosing the spatial grid that is used to translate the curvelets at each scale and angle. In this research the Wrapping based curvelet transform is used as it is faster in computation time and more robust than the USFFT based [36].

FDCT takes as input a 2D function of size MN and furnishes a set of coefficients $C^D(j,l,k)$ defined by:

$$C^D(j,l,k) = \sum_{m,n} f(m,n)\varphi^D(j,l,k) \tag{3.4}$$

Where $f(m,n)$ is the signal under analysis, $0 \leqslant m \leqslant M-1$, $0 \leqslant n \leqslant N-1$ define the coordinates on the Cartesian grid. $\varphi^D(j,l,k)$ is the curvelet basis function, j is the scale, l is the orientation and k is the spatial location . By varying k the curvelet function is translated, and the whole 2D space is covered. In addition, by varying
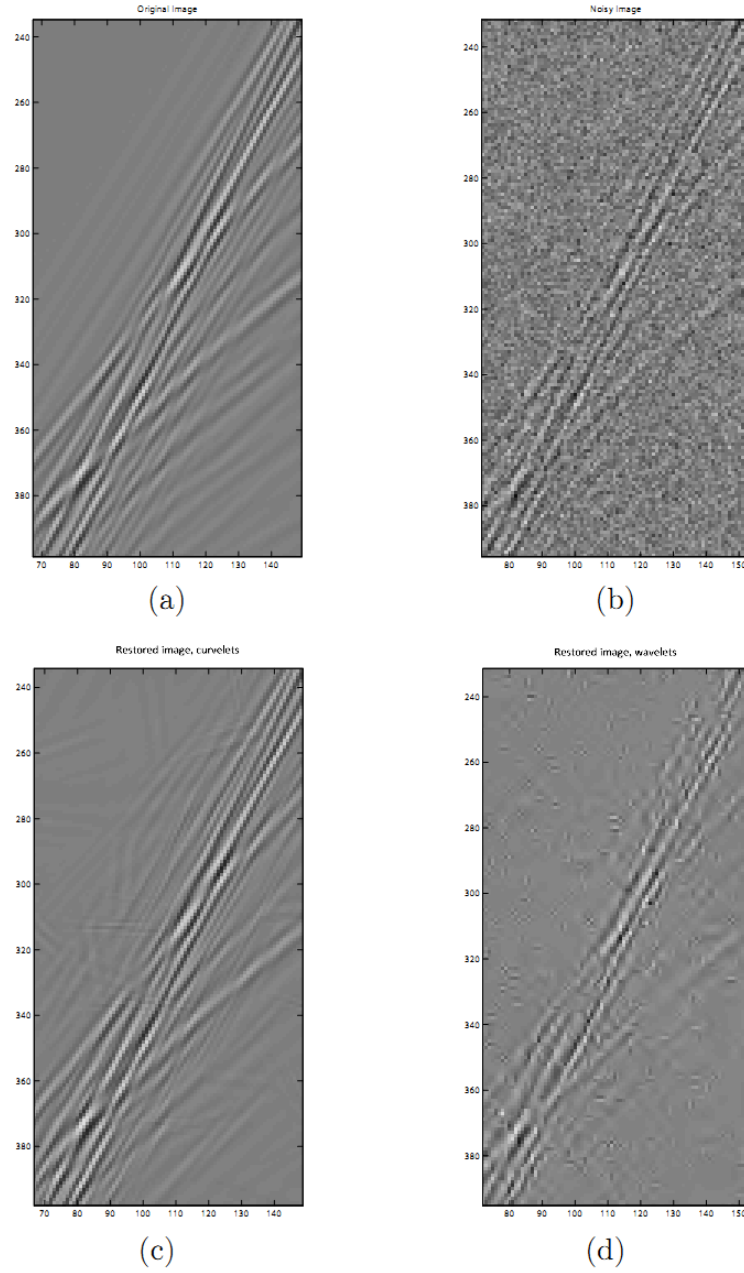
Fig. 3.9 Image denoising a) The Original image (zoom). b) Noisy image with Gaussian white noise. c) Denoised image using curvelets. d) Denoised image using wavelets [36]

j and l the function is tuned to different scales and orientations. By doing all this simultaneously, the curvelet transform covers the whole frequency spectrum so that there is no loss of information. The total number of scales depends on the size of the image and is given by

$$J = \lceil log_2(min(M, N)) - 3 \rceil \tag{3.5}$$

where $\lceil * \rceil$ is the ceiling function, and M and N are the number of vertical and horizontal image pixels respectively. Each scale is divided into L orientations (wedges):

$$L = nb \times 2^{\lceil (j-2)/2 \rceil} \tag{3.6}$$

where $j=2\ldots J$ and nb is the number of angles in the second coarse scale, which mostly is chosen to be a power of 2. Note that the coarsest level ($j=1$) is not directional. Its effect is similar to a low pass filter. One example of curvelet tiling and covering of spectrum of a $[256 \times 256]$ image with 4 directional scales on dyadic concentric square coronae and $nb = 8$ can be seen in Fig. 3.10. The shaded trapezoid (i.e. wedge-area) shows the frequency response at orientation 4 and scale 4.
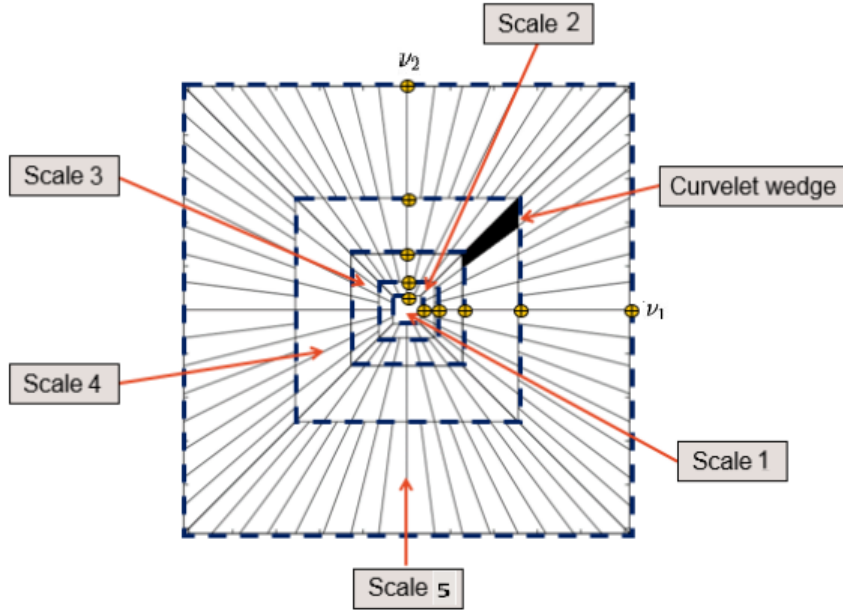
Fig. 3.10 Discrete curvelet tiling in the frequency domain [44]

3.2.5   FDCT Algorithm via Wedge Wrapping

The architecture of the FDCT via wrapping is expressed as Algorithm 1:

The complete transform process using a single curvelet is illustrated in Fig.3.11 [36].

There is a problem in applying inverse FFT on the obtained frequency spectrum. The frequency response of a curvelet is a non-rectangular wedge, then the wedge needs to be wrapped into a rectangle to perform the inverse Fourier transform. The wrapping is done by periodic tiling of the spectrum using the wedge, and then collecting the

---

Algorithm 1 FDCT via Wedge Wrapping

1: Take the FFT of the image and obtain Fourier samples $\widetilde{f}$.
2: Divide the frequency spectrum into a collection of Digital Corona Tiles (Fig. 3.10)
3: For each scale j and angle l:

    a. Form the product $\widetilde{U_{j,l}}.\widetilde{f}$ where $\widetilde{U}$ is the curvelet window.

    b. Wrap this product (the parallelogram shaped support of the tile) around a rectangle centered at the origin to obtain $\widetilde{f_{j,l}}$ (Fig. 3.11(b))

    c. Take the inverse FFT of the wrapped support $\widetilde{f_{j,l}}$ hence collecting discrete coefficients.
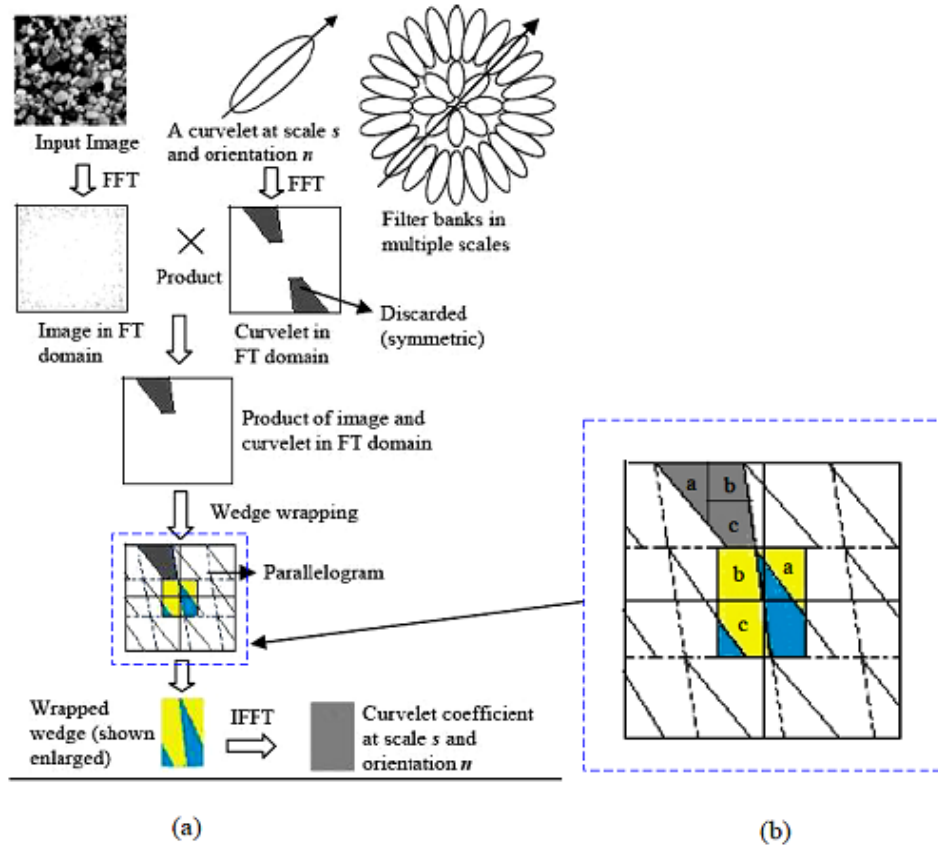
Fig. 3.11 a) Feature extraction process using a single curvelet b) Wrapping transformation [45].

rectangular coefficient area in the center. Through this periodic tiling, the rectangular region collects the wedge's corresponding portions from the surrounding periodic wedges. For this wedge wrapping process, the mentioned approach of curvelet transform is known as the 'wrapping based curvelet transform'. The wrapping is illustrated in Figure Fig. 3.11(b). As shown, in order to apply IFFT on the FT wedge, the wedge

has to be arranged as a rectangle. The idea is to replicate the wedge on a 2-D grid, so a rectangle in the center captures all the components a, b, and c of the wedge. Wedge wrapping is done for all the wedges at each scale in the frequency domain, so we obtain a set of sub bands or wedges at each curvelet decomposition level. These sub bands are the collection of the discrete curvelet coefficients [45].

3.2.6   Using FDCT Coefficients to Identify Important Directions

The values of curvelet coefficients are determined by how they are aligned in the real image. The more accurately a curvelet is aligned with a given curve in an image, the higher is its coefficient value. A very clear explanation is provided in Fig. 3.12. The curvelet named 'c' in the figure is almost perfectly aligned with the curved edge and therefore, has a high coefficient value. Curvelets 'a' and 'b' will have coefficients close to zero as they are quite far from alignment. It is well-known that a signal localized in frequency domain is spread out in the spatial domain or vice-versa. A notable point regarding curvelets is that they are better localized in both frequency and spatial domain compared to other transforms. This is because the wedge boundary is smoothly tapered to avoid abrupt discontinuity.

The obtained coefficients from the curvelet transform of an image are collected in a cell structure which is called C cell. These coefficients are used to extract the important directions in different locations of the image.

For example, the curvelet transform was applied on the image of FEM solution of the mentioned free space problem (section 3.1.1) with h=0.2λ and $\theta_i = 15°$ and 80°. The size of the image is $[256 \times 256]$ as shown in Fig. 3.2 and according to 3.5 the curvelet coefficients were obtained in 5 scales.

The cell structure of the image can be seen in Table 3.3. The coefficients of the 5 scales are presented in 5 different cells. Additionally, the cell of each scale is separated to different number of matrices which are related to different number of orientations in each scale. As shown, the total number of orientations in the coarsest scale was defined to be 132 to gain better orientation resolution. According to (3.6), this number is used for orientation division in other scales.

The coefficients of the second scale are selected for analysis regarding the spatial frequency content of the problem. As can be seen in Table 3.4, the cell of this scale includes 132 matrices that represent one matrix for each specific orientation.

To identify the important wave directions in the image, the energy of the 132 orientations in the second scale has been analyzed as shown in Fig. 3.13. The number of the 6 most energetic directions are $[80, 14, 15, 81, 56, 122]$, with the directions equal to
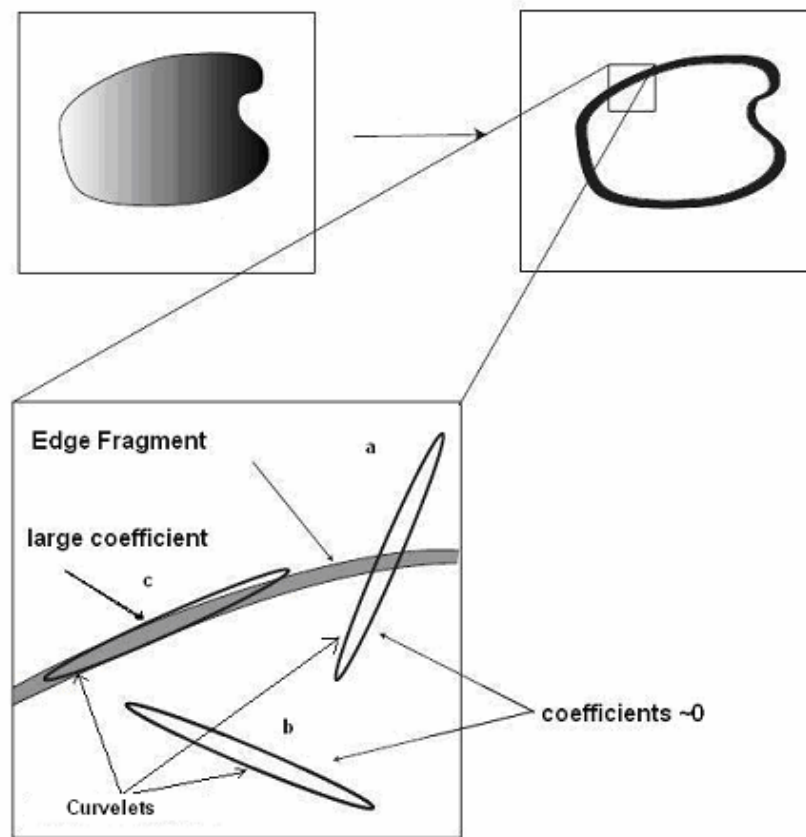
Fig. 3.12 Alignment of curvelets along curved edges [37]

Table 3.3 Curvelet coefficients distribution of the FEM solution of the free space problem

5 level decomposition				
C	$[1 \times 5]$ cell			
scale 1	scale 2	scale 3	scale 4	scale 5
$[1 \times 1]$ cell	$[1 \times 132]$ cell	$[1 \times 264]$ cell	$[1 \times 264]$ cell	$[1 \times 528]$ cell

Table 3.4 Curvelet coefficients distribution at second scale C{1,2}

scale 2	$[1 \times 132]$ cell			
number of directions	1 to 33	34 to 66	67 to 99	100 to 132
angle of directions (deg)	⟨45 to −45⟩	⟨315 to 225⟩	⟨225 to 135⟩	⟨135 to 45⟩

$[260.45°, 80.45°, 83.18°, 263.18°, 195°, 15°]$ respectively. In comparison to the identified directions using FFT analysis which are equal to $[16°, 82°]$, the direction resolution of the curvelet transom is better than the FFT.
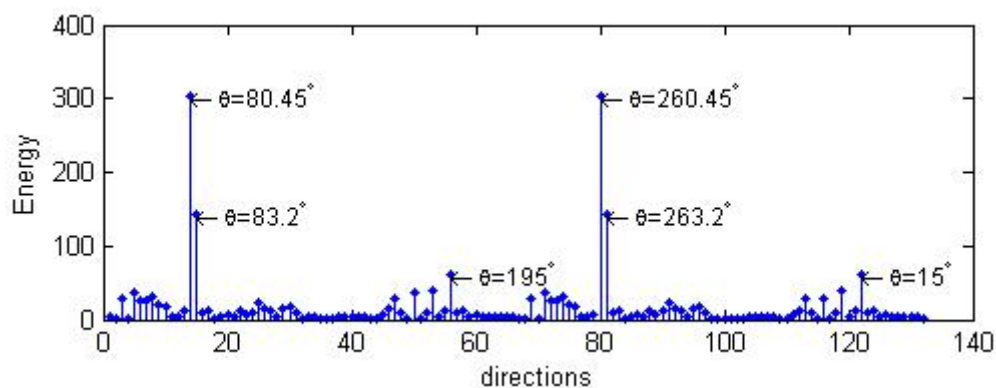
Fig. 3.13 Energy distribution of curvelet coefficient of the image in second scale

The next step is the extraction of the location information of the important wave directions in the original image. This information could be found by analyzing the matrix of the identified directions. For example, the $122th$ matrix in the second scale was analyzed to find out where in the original image the waves with direction $15°$ exist. The matrix size for this orientation is C{1,2} {1,122} = $[3 \times 16]$. It means that the whole image is divided to $3 \times 16 = 48$ different parts and then the mentioned curvelet (with specific orientation and scale) is applied to each part to achieve the coefficients in different locations of the image. This curvelet in different parts of the image is shown in Fig. 3.14. As can be seen, each curvelet cover the whole image in space domain and therefore, there is no loss of information in space domain.

Consequently, the amount of the 48 coefficients in the mentioned matrix are compared to determine the greater ones. Finally, the pixels of the original image related to the identified curvelet positions are determined. The identified locations in the original image can be seen in Fig. 3.15. The identified directions and the location information of them are used to determine specific enrichment functions configuration for each node in the GFEM solution. The Details of the pre-processing methodology is described in chapter 4.

Fig. 3.14 A single curvelet in different locations of the image, identified wave direction = 15°, second scale

Fig. 3.15 Identified locations of the important wave directions a) wave direction = 15°, b) wave direction = 195°
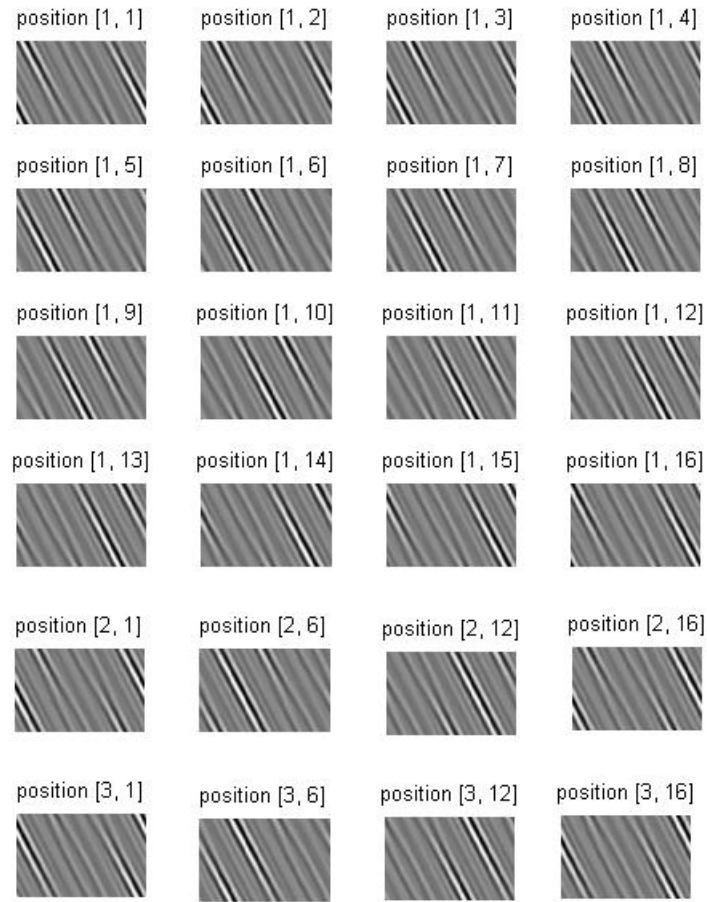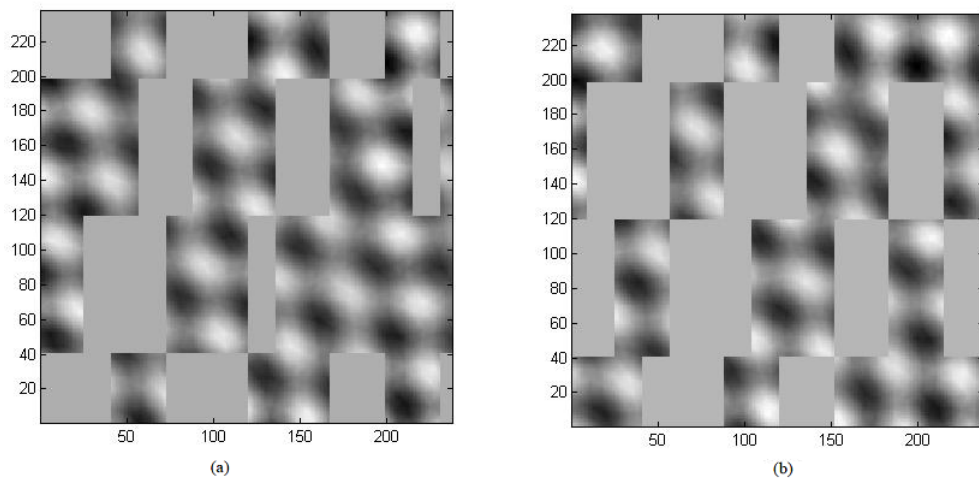
Chapter 4

Proposed Methodology and Results

4.1 Defining the Extents for the Number of Wave Directions for GFEM Using FFT

As mentioned previously, the number of wave directions and the set of distributed angles are important in the GFEM enrichment. A low number of enrichment functions will lead to low quality solutions. On the other hand, a high number of wave directions will lead to ill-conditioned systems and also to low quality solutions. A suitable distribution could be selected considering the DFT analysis.

To illustrate the influence of the enrichment function orientation in the GFEM, the free space problem was solved for different incident waves, θ_i from 0° to 90°. For each θ_i, the most important wave direction was obtained from the FEM solution applying the FFT approach and it was used to rotate the enrichment wave distribution. Thereafter, the problem was solved using GFEM with $q = 2, 4$ and 8. Results for the $h = 0.2\lambda$ mesh are presented in Fig. 4.1 in which the error function is measured using the relative $L^2(\Omega)$-norm error as described in (2.40).

As can be seen in Fig. 4.1, at $\theta_i = 0^o$, standard GFEM with $q = 2$ produces errors smaller than FEM by several orders of magnitude. This error increases as the incidence angle of the wave differs from those used in the enrichment functions which are equal to $\theta_{l_1} = 0^o$ and $\theta_{l_2} = 180^o$ as described in section 2.1.5 and Fig. 2.3. Even using a poor mesh, FEM performs better than GFEM at $\theta_i = 90^o$ because in this configuration the incident wave is perpendicular to both waves used as enrichment functions.

In contrast, solving the problem by GFEM yields smaller errors when the standard enrichment function distribution is rotated. The error is kept to a small value, determined mainly by the accuracy of the angle found through the FEM solution. The deep
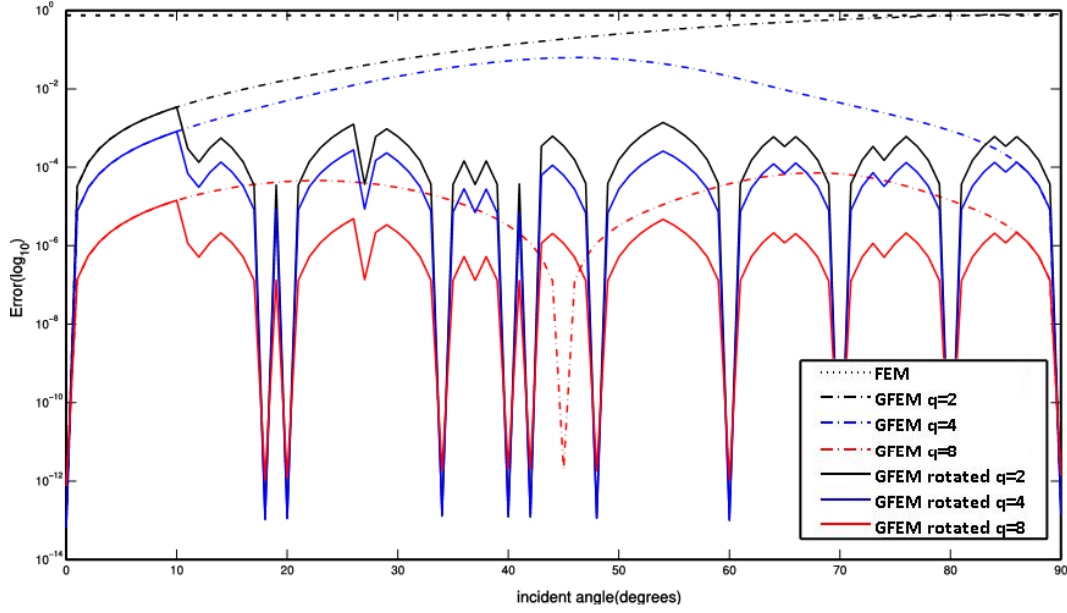
Fig. 4.1 Error comparison between GFEM with traditional and rotated directions as a function of θ_i for $q = 2$, $q = 4$ and $q = 8$

valleys in Fig. 4.1 represent instances of the problem where the rotation angle matched perfectly the incidence angle.

A comparison between GFEM standard errors by different number of wave directions indicates that $q = 4$ is more accurate than $q = 2$ and the best results is obtained when $q = 8$. Using $q = 4$ improves the error at $\theta_i = 90^o$, remaining below the FEM result. The rotated GFEM with $q = 4$ has a better accuracy than the traditional one, besides the additional rotated wave directions contribute to an improvement in the error quality of the results. The minimum error is obtained by GFEM with eight rotated wave directions.

In addition, when the identified angle from DFT procedure matches the incident angle, the quality of the solution reaches the numerical precision and the rotated GFEM is independent of the number of wave directions. Otherwise, additional waves can be useful to compensate the inaccuracy of the DFT procedure. However, there is a limit for the error reduction since the increasing of q could lead to ill-conditioned solutions.

4.1.1   Procedures to Extract the Extents for the Number of Enrichment Functions

Theoretically, any integer can be used as the number of enrichment function. However using Fourier analysis, it is possible to define an appropriate range for the number of

wave directions (4.1) in which the quality of the GFEM solution is guaranteed.

$$q_{min} \leq q \leq q_{max} \tag{4.1}$$

4.1.1.1 The Upper Limit for the Number of Wave Directions

As can be seen in Fig.4.1 the smaller errors are related to the greater number of wave directions. However using too many directions does not ensure to more accurate results. This means that there is a limit for the maximum number of wave directions in each problem. After that amount, by increasing q, the error would be increased likewise. This limit can be determined by considering the Nyquist sampling criterion in (3.1) and the maximum resolution of the DFT analysis (3.3).

According to (3.3) the maximum number of frequency components which is achievable by DFT is MN, where M and N are the number of sample points in each direction in a 2-D image. If M and N respect the Nyquist criterion, the image can be reconstructed without loss of information.

However, since the image in this research is periodic functions of the Helmholtz equation, most of the MN spectral components in (3.3) vanish. Only the components lying inside the spatial mask contribute to the correct reconstruction of the solution. As a result the total achievable resolution, or equivalently, the maximum acceptable number of wave directions can be calculated by (using the formulation of the ellipse circumference):

$$q_{max} = 2 \cdot \pi / 4 \left(\sqrt{\frac{\left(\frac{D_x}{\lambda/2}\right)^2 + \left(\frac{D_y}{\lambda/2}\right)^2}{2}} \right) = 1.11 \sqrt{(2(D_x/\lambda))^2 + (2(D_y/\lambda))^2} \tag{4.2}$$

In which Dx and Dy are the domain sizes in x and y directions respectively and q_{max} is the maximum number of wave directions which is related to the minimum error.

4.1.1.2 The Lower Limit for the Number of Wave Directions

As discussed in the previous section, the information about the most important wave directions could be obtained a priori by solving the problem using the FEM with the same coarse mesh that will be used in the GFEM. In this case, the number of peaks identified in the 1-D DFT calculations could be used as an approximation for the minimum required number of wave directions (q_{min}). It is noteworthy that the DFT is a complex valued function of spatial frequency. However the information about the effective directions was extracted from the absolute value of the 2-D DFT results, as can be seen in Fig. 3.3. Therefore, to cover the information about the argument part

of the DFT results, for each identified direction, there should exist another one in the opposite direction. This means that, for a small number of wave directions, if an odd number is identified through the DFT analysis, the next even number should be selected as q_{min}. Whereas for q_{max}, as a result of the existence of angles near to the opposite directions for each angles, there is no need to verify the parity.

4.1.2   Setting the Enrichment Functions Distribution

Using the wave directions obtained from the DFT could lead to inaccurate results due to the noise generated by the low quality mesh. In this context, uniformly distributed directions clustered around the identified angles are used to have more accurate results. This procedure is based on the fact that the ill-conditioning is directly related to the angle between the wave directions [15]. Generally, the condition number increases when the difference between the directions decreases and also when the number of the small angle differences increases. This content results from the simulations which have been done for different problems. The pollution error is better when the equally distributed wave directions is used for GFEM solution in comparison to the other types of the plane waves distributions.

There are several ways to generate uniform distributed directions based on the information obtained with the DFT. In this work, the minimal angle between the peaks $d\theta$ is used to estimate the number of enrichment functions $q = \lfloor 2\pi/d\theta \rfloor$. This number should meet the extents in (4.1). If the resulted q is greater than the upper limit then the second minimal angle is used to calculate the q. This procedure is continued until a feasible q is found. Furthermore, if q is smaller than the q_{min}, the mean of the lower and upper limit is used. Finally the highest peak angle is applied to rotate the distribution

4.2   Results Using FFT

The free space problem, a perfect conductor scattering problem and the multiple circular scatter problem were used to verify the ability of the proposed methodology in identifying the acceptable region for the number of wave directions in GFEM configuration. In these three problems, solutions are given in terms of the Transverse Electric (TEz) field. The excitation is imposed using the first order absorbing boundary condition (ABC) at the artificial boundaries, assuming different incident waves. The

numerical integration in the FEM and GFEM equations are performed using 100 Gauss points in triangle elements and 10 Gauss points in the line elements.

The mentioned problems can be seen as a part of more complex problem composed by some far field regions (with a main direction of propagation) and some near scattering regions (with many interfering waves).

4.2.1   Free Space Problem

The problem is analyzed with $\theta_i = 15^o$ and $h = 0.2\lambda$. After applying DFT on FEM solution, only one peak occurrence was detected at $\theta = 18^o$ as shown in Fig. 4.2. Therefore the minimum number of wave directions that could be used in the GFEM configuration in this problem is $q_{min} = 2$. On the other hand, the upper limit according to (4.2), assuming $D_x = 6$, $D_y = 3$ and $\lambda = 1$, is $q_{max} = 15$. As a result, the number of wave directions should be selected between 2 and 15 and also the main directions has to be $\theta = 18^o$.
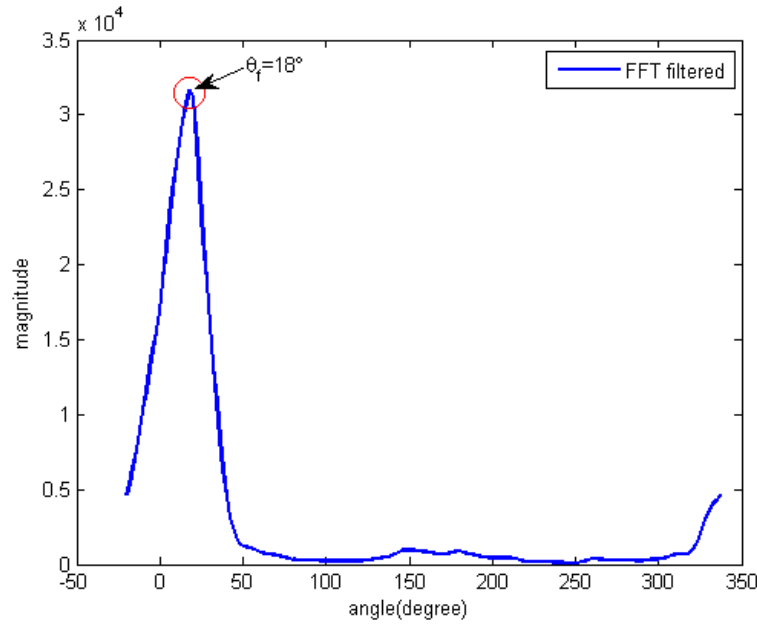

Fig. 4.2 1-D problem obtained after the filtering process, Mesh size $h = 0.2\lambda$, $\theta_i = 15°$.

Fig.4.3 illustrates the GFEM convergence as a function of q. It shows that the error decreases when q increases from 2 to 15 and the minimum error occurred at $q = 15$. After this limit, the error increased despite the increment in the number of wave directions.
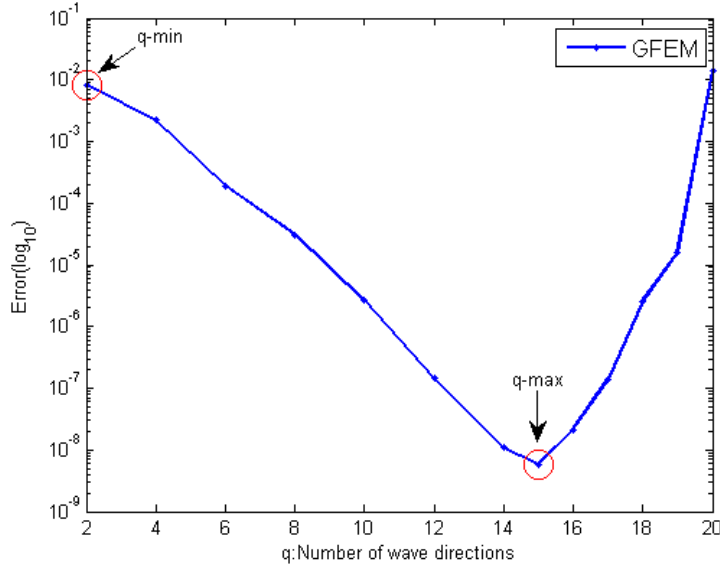
Fig. 4.3 GFEM convergence for the free space problem, mesh size $h = 0.2\lambda$ and $\theta_i = 15°$.

4.2.2 Perfect Conductor Scattering Problem

To simulate a more complex field behavior, a L-shape reflector is used. The wave number is defined as $k = 2\pi$ for the two discretized domains presented in Fig. 4.5. The first mesh is composed of 250 nodes ($h = 0.5\lambda$) while the second one is composed of 426 nodes ($h = 0.4\lambda$).
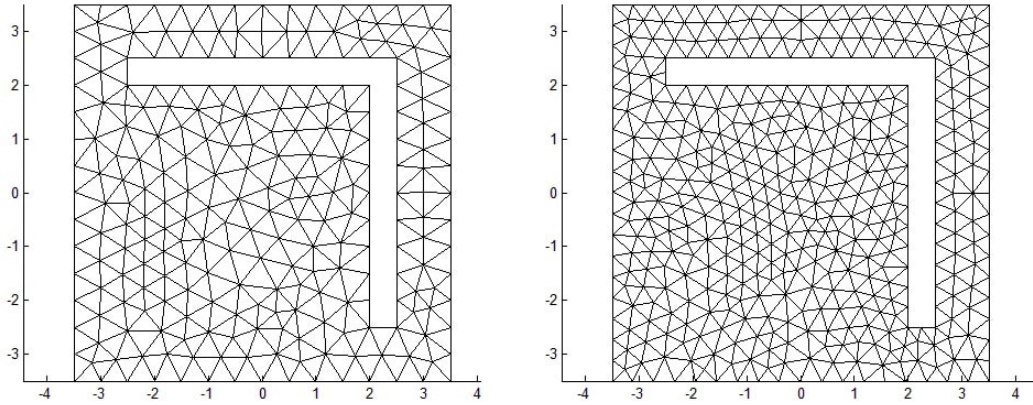
Fig. 4.4 Domain discretization a) Mesh size $h = 0.5\lambda$, b) Mesh size $h = 0.4\lambda$

Using the $h = 0.4\lambda$ mesh and an incident wave with $\theta_i = 30^o$, the DFT procedure identifies five main components in the FEM solution $\theta_{fem} = [26\ 36\ 206\ 216\ 326]$,

resulting in $q_{min} = 6$ as can be seen in ??. The upper limit, $q_{max} = 22$, is defined according to (4.2) considering $D_x = D_y = 7$ and $\lambda = 1$.

Fig. 4.5 Identified wave directions using DFT, $\theta_i = 30^o$, $h = 0.4\lambda$

The relative $L^2(\Omega)$-norm error for FEM, GFEM and GFEM with rotated directions are presented in Fig. 4.6 as a function of 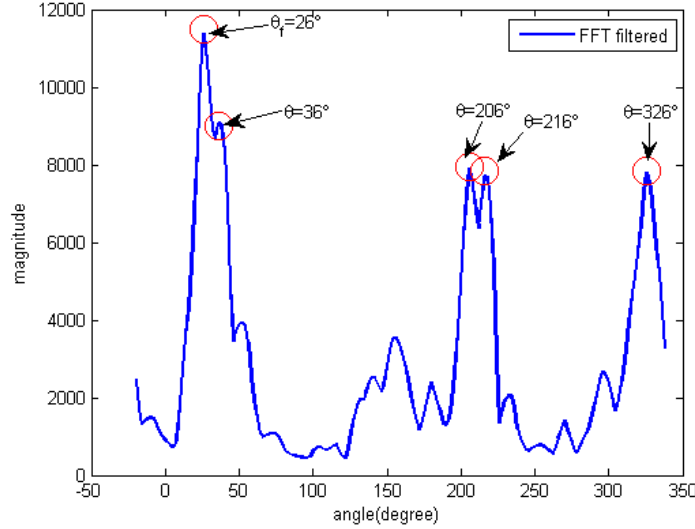the number of degrees of freedom NDOF. It should be mentioned that because there is no analytic solution for the reflector problem, a very fine mesh FEM solution (131,566 nodes) is regarded as a reference to calculate the error for this problem.

As can be seen, the error for GFEM solutions are smaller than the FEM solution for the same NDOF. Additionally, both GFEM solutions present quite similar behavior. In both cases the error decreases when q increases from 2 to 6, then for $q = 6$ to $q = 22$ (shaded area) the error is approximately constant and minimum despite the increment of q and finally at the third part of the figure the error increases when the q increases.

The shaded area matches with the extends defined in (4.1). As expected, for $q > q_{max}$ the increase in the number of enrichment functions has not positive influence on the quality of the solution, in addition, it has a strong influence in the condition of the matrix. The condition number of the matrix as a function of q is presented in Fig. 4.7. Since the standard and the rotated enrichment procedure uses equally spaced directions, both results are quite similar.

Moreover, different from the free space problem (Fig. 4.1), the influence of the rotation of the enrichment functions is very small since the number of wave components existing in the problem is considerably high.
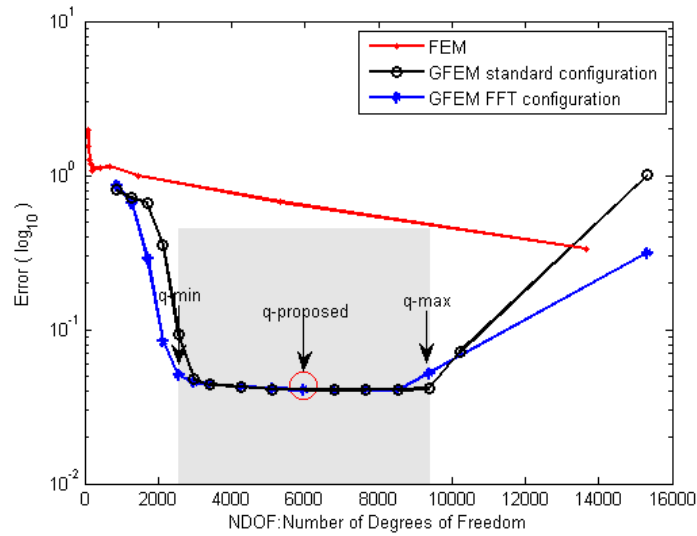
Fig. 4.6 Error comparison between FEM, GFEM with equally spaced and GFEM with selected directions, $\theta_i = 30^o$, $h = 0.4\lambda$

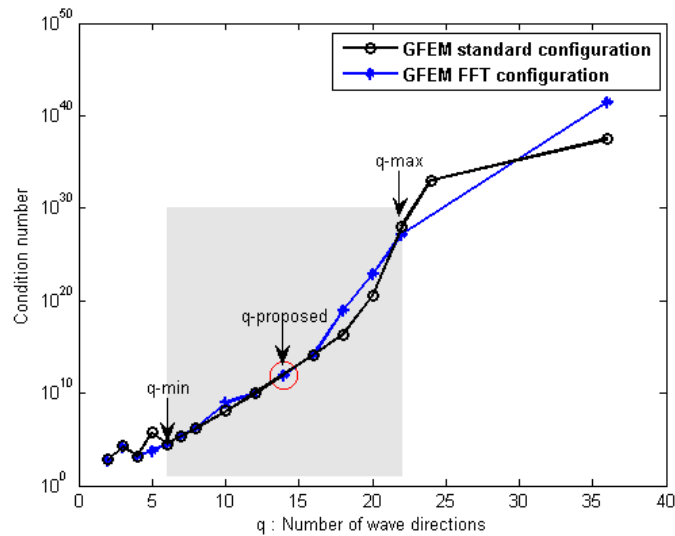Fig. 4.7 Condition number in different number of wave directions for GFEM with equally spaced and GFEM with selected directions, $\theta_i = 30^o$, $h = 0.4\lambda$

According to the procedure (described in section 4.1.2) for creating equally spaced directions, $q = 14$ is selected as the number of wave directions and $\theta = 26^o$ is applied to rotate the distribution.

The comparison between the quality parameters of GFEM solution with proposed configuration using FFT analysis and also the configurations with minimum and maximum number of wave directions can be seen in table 4.1.

Table 4.1 Comparison of GFEM solution using FFT analysis with different numbers of the wave directions, $\theta_i = 30^o$, $h = 0.4\lambda$

Number	$q_{proposed} = 14$	$q_{min} = 6$	$q_{max} = 22$
NDOF	5964	2556	9472
Error	0.0407	0.0507	0.0523
Condition number	$8.53 * 10^{11}$	$3.17 * 10^{4}$	$1.42 * 10^{27}$
Running time(sec)	2341.59	854.02	5622.76

It is shown that, if the q_{max} is used, the GFEM solution would result in the maximum condition number in the identified region. On the other hand, the error of the GFEM solution with q_{min} is considerably greater than the error of the GFEM with proposed q. Whereas, the minimum error in the acceptable area is related to the proposed configuration along with the average number of the degrees of freedom and the moderate condition number. It means that by using the proposed GFEM configuration it is possible to reach the near optimal solution in the mentioned area with smaller computational cost in comparison to the traditional GFEM solution.

The problem was also solved using the mesh with size $h = 0.5\lambda$ and a incident angle of $\theta_i = 60^o$. Since the upper limit of q is independent of the mesh size, it remains unchanged. However, the lower limit changes to $q_{min} = 8$ due to the differences in the incident wave and the quality of the initial FEM solution. The relative $L^2(\Omega)$-norm error and the region with the limits of q are presented in Fig. 4.8. It shows that the minimum error occurs inside the region defined by (4.1).

Setting the enrichment distribution according to the procedure described in section 4.1.2, the third minimal distance between the identified angles is used to determine the number of wave directions used as enrichment function ($q = 16$). Then, the set of plane waves is rotated to match the wave component with the highest energy $\theta = 52^o$.

4.2.3   Multiple Circular Scatter Problem

To verify the proposed method with a complex problem, an array of circular scatters is analyzed with $\theta_i = 30^o$, $h = 0.1\lambda$ and $k = 2\pi$. The mesh is composed of 11094 triangular elements, resulting in 626 edges and 5852 nodes. The method of fundamental solutions (MFS) with Neumann boundary condition is used as a reference for this problem
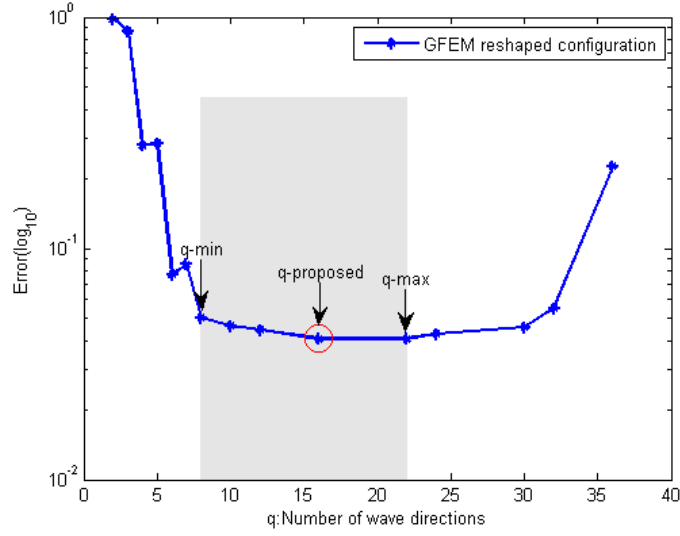
Fig. 4.8 Error of GFEM with reshaped distribution,$\theta_i = 60^o$,$h = 0.5\lambda$

[46].The MPSpack [47] solution of the problem, which solves 2D scattering problems to machine precision, can be seen in Fig. 4.9.
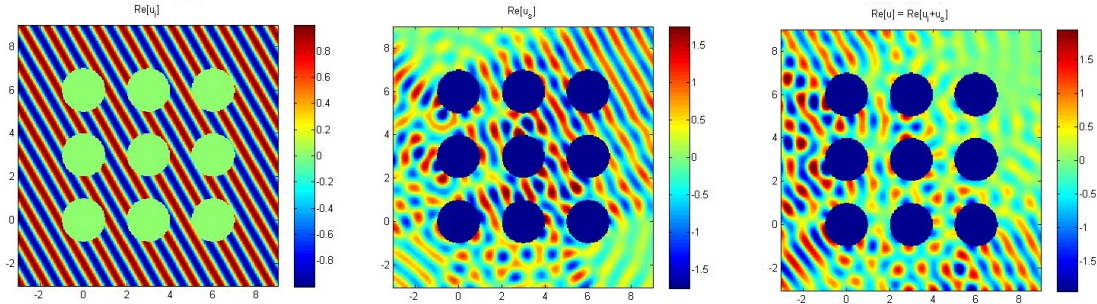
Fig. 4.9 disc array scattering, Left: incident wave. Center: scattered wave. Right: total solution field,$\theta_i = 30^o$, $h = 0.1\lambda$

After applying DFT on FEM solution, only one peak occurrence was detected at $\theta = 30^o$ as shown in Fig.4.10. Therefore the minimum number of wave directions that could be used in the GFEM configuration in this problem is $q_{min} = 2$. On the other hand, the upper limit according to (4.2), assuming $D_x = 12$, $D_y = 12$ and $\lambda = 1$, is $q_{max} = 38$.

The problem is solved using the $q = 4$ which is in the identified range and rotated configuration with one direction aligned to $\theta = 30^o$. The real and imaginary part of the electric field along $C_x = \{(x,y) \,|\, y = 0, -3 \leqslant x \leqslant 9\}$ for GFEM rotated and MFS solution can be seen in the Fig.4.11 and Fig.4.12. In addition, the solution with fine mesh
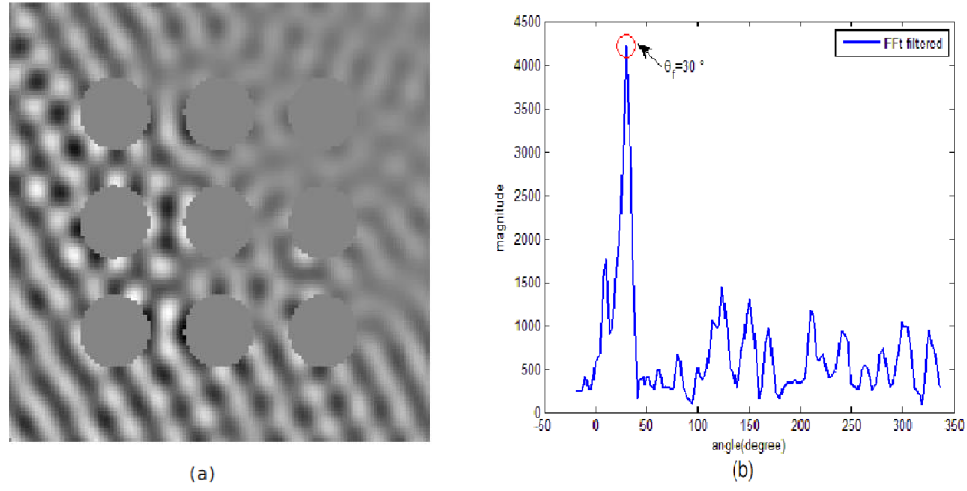
Fig. 4.10 a) Image of FEM solution , b) Obtained direction using 1-D FFT for $\theta_i = 30^o$, $h = 0.1\lambda$

$h = 0.02\lambda$ using FEM and GFEM standard with $q = 4$ can be seen in the mentioned figure.
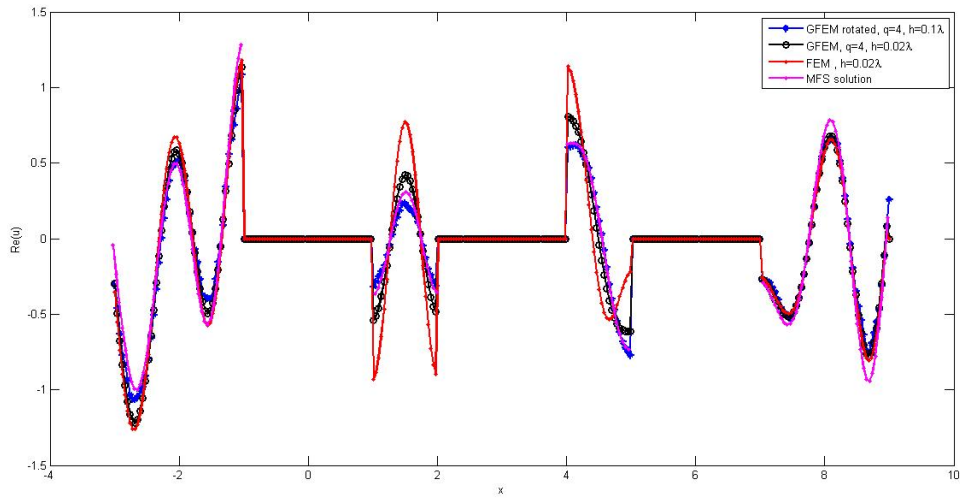
Fig. 4.11 Real part of electric field along $C_x, \theta_i = 30^o$, using FEM, GFEM rotated, GFEM standard and MFS

The comparison between the quality parameters of GFEM solution with proposed configuration using FFT analysis and also the GFEM and FEM with fine mesh can be seen in table 4.2.

It is observed that smaller error is achieved by the GFEM rotated solution on coarse mesh in comparison to standard GFEM and FEM solution on fine mesh. It means
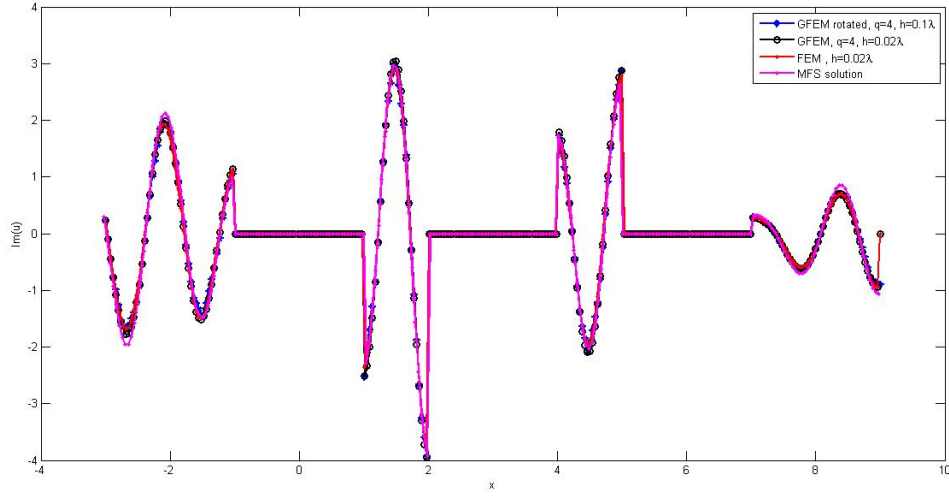
Fig. 4.12 Imaginary part of electric field along $C_x, \theta_i = 30^o$, using FEM, GFEM rotated, GFEM standard and MFS

Table 4.2 Comparison of GFEM rotated, GFEM standard and FEM solution for disc array scatter problem, $\theta_i = 30^o$,

Method	GFEM Rotated	GFEM	FEM
Mesh size	$h = 0.1\lambda$	$h = 0.02\lambda$	$h = 0.02\lambda$
Number of directions	$q = 4$	$q = 4$	-
NDOF	23408	540840	135210
Error	0.0684	0.0720	0.0876
Condition number	$1.15 * 10^5$	$6.35 * 10^{563}$	$1.15 * 10^5$
Running time(sec)	1006.36	5 days	2950.72

that, by using the identified angle as the main direction of the configuration and with small number of wave directions, a good approximation to the reference solution can be achieved. Additionally, the proposed method leads to smaller condition number and time saving compare to the GFEM and FEM with fine mesh.

4.3   Identifying the Optimum Configuration for GFEM Solution Using the Curvelet Transform

The analysis of the Discrete Fourier Transform of the FEM solution of a problem is useful to find the directions of the present waves. The extracted information would

be used to determine suitable configuration for GFEM solution of the problem. As
indicated in the previous section, the results showed that even on very poor meshes
($h \to 0.5$) it can result on accurate and converging GFEM solutions.

Although the previous approach define the range of q for the accurate GFEM
solution, it lacks definition of the optimum number of wave directions in this range. In
addition, it is not possible to define where the identified directions has existed in the
space domain of the problem.

In this section it is proposed alternatively, to use the curvelet transform to achieve
local information of important wave directions in the domain space and therefore
identify how many wave directions are necessary to cover all the domain. The identified
number would be used as the optimum number of wave directions q_{opt} for all nodes
in GFEM solution in the first version of this approach. Additionally, the presented
approach leads to improvements in the condition number and computational cost of
each problem as a result of reduction in the total number of degrees of freedom.

4.3.1   Extract Optimum Configuration Applying FDCT

The proposed idea in this research is to apply the curvelet Transform on the coarse-mesh
finite element solution to extract useful information a priori about wave directions in
GFEM configuration. It should be noted that the appropriate size for the FEM mesh
(also used as the GFEM mesh) is selected considering the Nyquist sampling theory.
The acceptable coarse mesh size should be smaller than half of the minimum existent
wavelength. The proposed algorithm can be summarized as follows:

**Algorithm 2 : Extract optimum GFEM configuration using FDCT via wrapping
technique**

1: Choose the coarse mesh size considering the Nyquist sampling limit
2: Take FEM solution of the coarse mesh to obtain grid data
3: Select the appropriate scale and angle decomposition as input parameters and then
   apply FDCT on the image of FEM data
4: Analyze the energy spectrum of curvelet coefficients in all the directions of the
   selected scale
5: Identify the most energetic directions in different parts of the image θ_{max}
6: Define the q_{opt} as the most energetic wave directions which is required to cover the
   whole image
7: Set the optimum configuration for each node in the mesh according to the q_{opt} and
   respective local identified directions
8: Solve the GFEM for coarse mesh considering the obtained configuration for each
   node

It should be noted that in step 3 the maximum number of scales of an image is given by (3.5). However, only the scales that matches spatial frequencies of the problem are necessary to define q_{opt}. Additionally, nb in (3.6) is defined such that L for the selected scales would be greater than 2 times of the maximum resolution of the problem (q_{max} in (4.2)). Finally, as described in step 7, the q_{opt} is used in (2.11) for all the nodes and the θ_l distribution in (2.16) is changed to $\theta_l = \theta_{max} + \frac{2\pi l}{q_{opt}}$, $l = 0, ..., q_{opt} - 1$. θ_{max} is different for each node of the mesh and is defined by the most energetic orientation l in the corresponding p node.

The flowchart of this algorithm can be seen in Fig. 4.13.
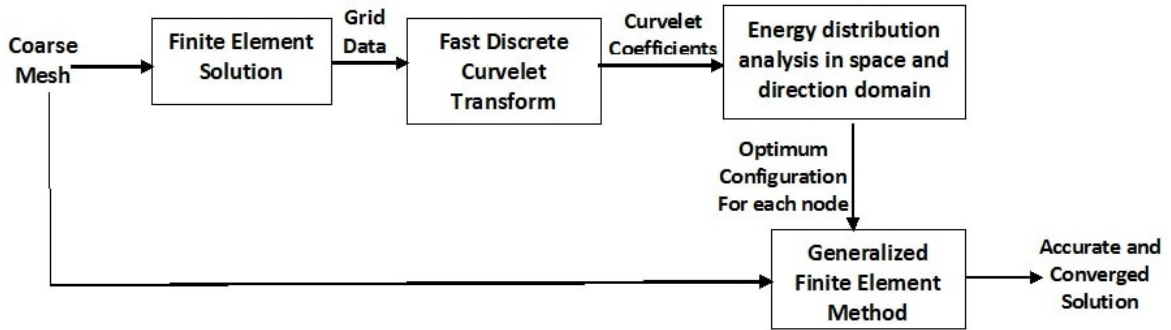
Fig. 4.13 The Proposed Algorithm for GFEM Solution of Coarse Mesh Using Curvelet Coefficients

4.4 Results Using Curvelet

4.4.1 Free Space Problem

An analytical solution of wave propagation in the free space domain $\Omega = \{(x,y), |-3.5 \leq x \leq 3.5|, |-3.5 \leq y \leq 3.5|\}$ with 4 different parts was used as an example to investigate the capability of curvelet in identifying the directions and locations. The wave number is set as $k = 2\pi$ and the incident angles are $\theta_i = 0^o, 90^o, 60^o$ and 30° for lower left, upper left, upper right and lower right corners, respectively. The TEz solution is shown in Fig. 4.14.

The total number of scales is 5, considering the image size (256×256). However, only the $3rd$ scale was selected for analysis as the spatial frequency component of the problem is located in the frequency range of this scale. The number of orientations for this scale should be greater than 2 times of 22 (due to the size of the domain and wave number of the problem). As a result, a FDCT grid with $nb=32$ was applied to
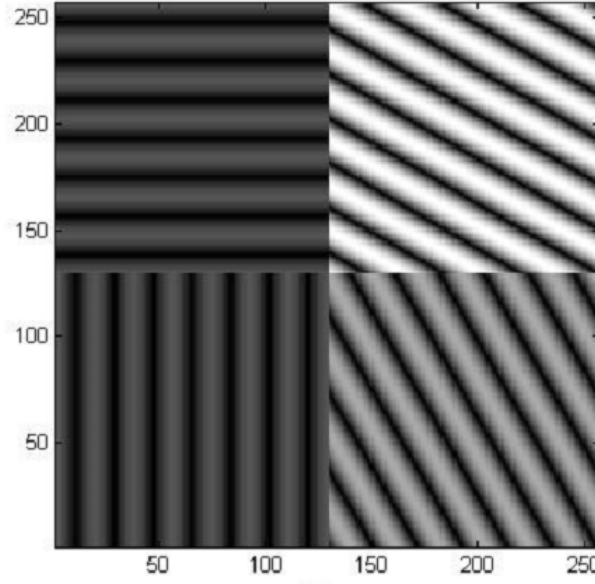
Fig. 4.14 Image of analytical solution with 4 different angles.

the image and the most important directions were identified by comparing the energy amount of the coefficients in the 64 directions (starts at $\theta = 45^o$) of scale 3 (Fig. 4.15).
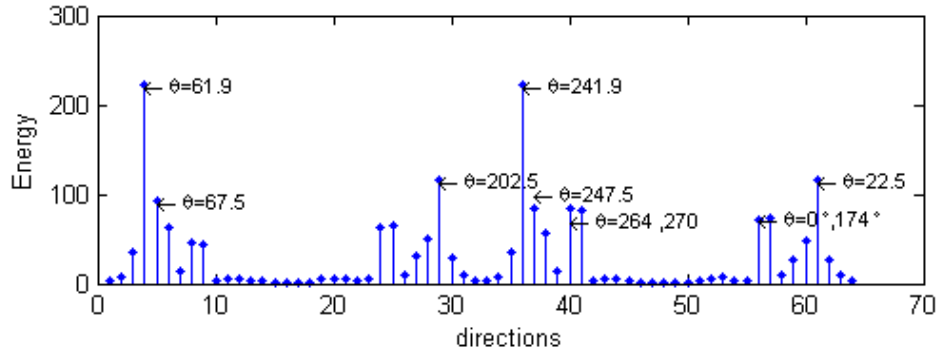
Fig. 4.15 Energy of each direction according to coefficient matrix of curvelet transform of the image

Finally, the pixels which are in the most correlation with each identified direction were identified and removed from the original image. This procedure was iterated until whitening the image.

As can be seen in Fig. 4.16, whitening the whole image was done using the first 10 most energetic directions. The angles of the identified directions are [61.9, 241.9, 22.5, 202.5, 67.5, 247.5, 264.4, 270, 0, 174.4], which were defined considering the orthogonality of the curvelet major axes in the frequency and space domains. For instance, the angles

of the two most energetic directions, numbers 4 and 36 in Fig. 4.15, are equal to 61.9^o and 241.9^o, which are close to one of the incident wave directions $\theta_i = 60^o$ and its opposite direction 240°. Moreover, the removed parts of the image, according to two first identified directions, which can be seen in the first two images of Fig.4.16, correspond well with the location of $\theta_i = 60$ at the right upper corner of the original image. It is evident that all the 10 locally extracted directions are in good agreement with the incident angles and their respective location in the analytical solution.
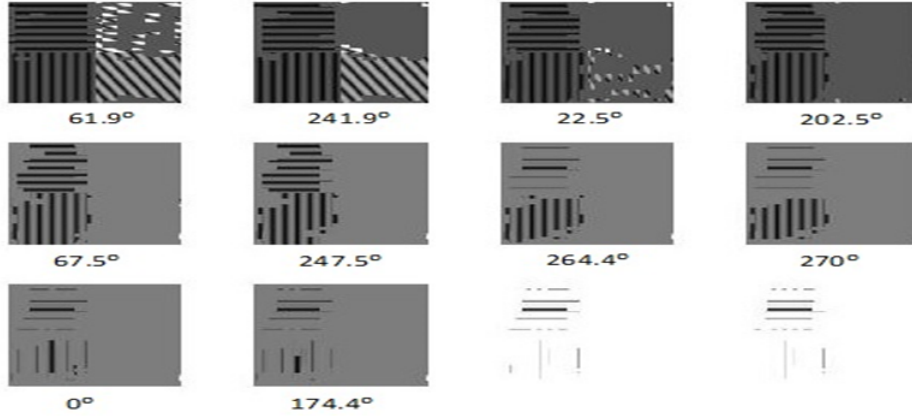

Fig. 4.16 Removed part of the image considering the most energetic directions

4.4.2   Perfect Conductor Scattering Problem

To assess the efficiency of the proposed methodology, the scattering problem of the L-shape reflector was used. The reflector was illuminated by an incident plane wave with an angle of incidence $\theta_i = 30^o$ and wave number $k = 2\pi$. As indicated in Fig. 4.17(a), the mesh is composed of 426 nodes ($h = 0.4\lambda$) and the image of FEM solution using this mesh is shown in Fig. 4.17(b). The solution is given in terms of the Transverse Electric (TEz) field.

According to (3.5) and the size of the image ($M = N = 100$), the 2-D frequency domain is divided into 4 scales. Regarding the frequency component of the problem, the most concentration of energy is in the second scale and $q_{max} = 22$. Therefore, the curvelet transform with $nb = 64$ was applied on the coarse mesh FEM solution and the energy in each direction in the second level were achieved as shown in Fig. 4.18.

In the next step, the most energetic directions were identified and the respective positions of these directions in the image were determined. Lastly, the pixels related to the most energetic coefficients were removed and the procedure was iterated until achieving the extant directions in the whole image. As it can be seen in Fig. 4.17(b), the
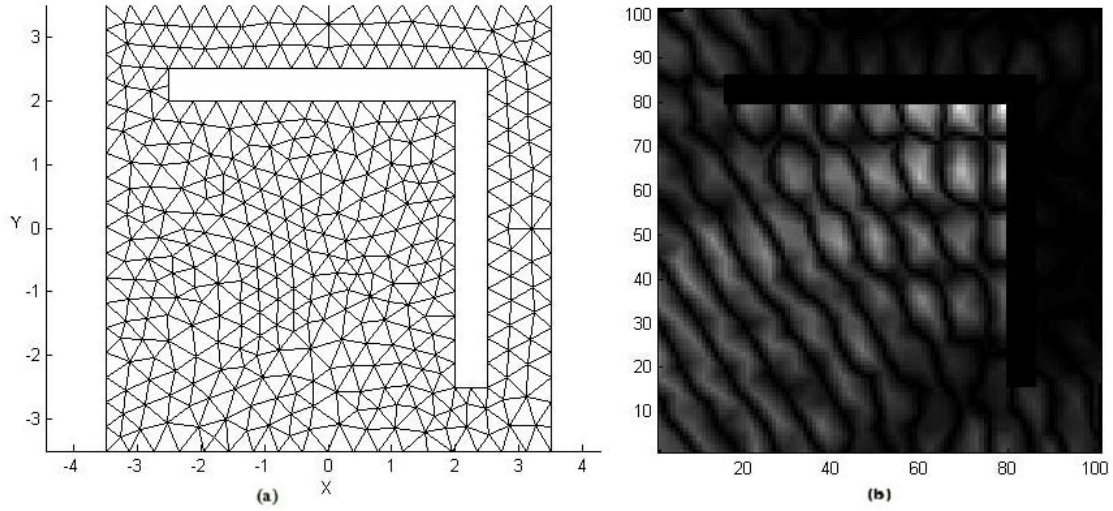
Fig. 4.17 a) Domain discretization, mesh size $h = 0.4\lambda$, b) Image of FEM solution
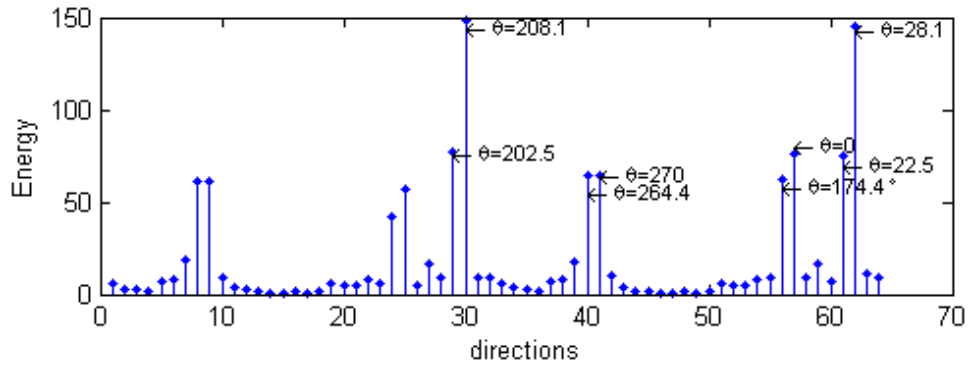
Fig. 4.18 Energy of directions

left lower corner of the image is more related to the incident wave $\theta_i = 30^o$. This part of the image showed the most correlation with curvelets number 30 and 62 (the two most energetic directions) whose angles are 208.1^o and 28.1^o, respectively, Fig. 4.19. Also it has been detected that curvelets number 4 and 12, with angles 0° and 270°, occurred more than other directions in the right upper corner. This is in conformity with the combination of incident and reflected waves at this corner. Finally, it was determined that the image whitening process could be completed by using only the 8 most energetic directions. As a result, 8 directions were sufficient to reach the information about FEM solution in the whole domain.

The identified directions were applied to the enrichment functions configuration of respective nodes in the coarse mesh and the problem was solved by GFEM with different numbers of wave directions. The relative $L^2(\Omega)$-norm error and condition
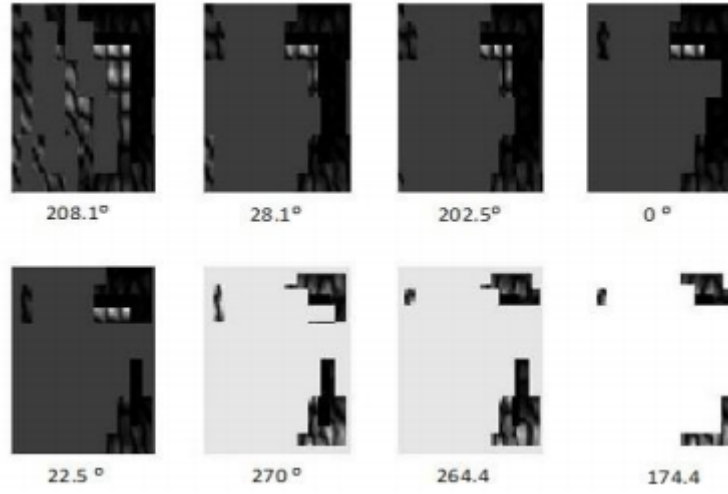
Fig. 4.19 Location of the most energetic directions

number for GFEM with traditional configuration and with identified directions using DFT and FDCT are presented in Fig. 4.20 and Fig. 4.21. It should be mentioned that because there is no analytic solution for the reflector problem, a very fine mesh FEM solution (131,566 nodes) is needed to calculate the error for this problem.
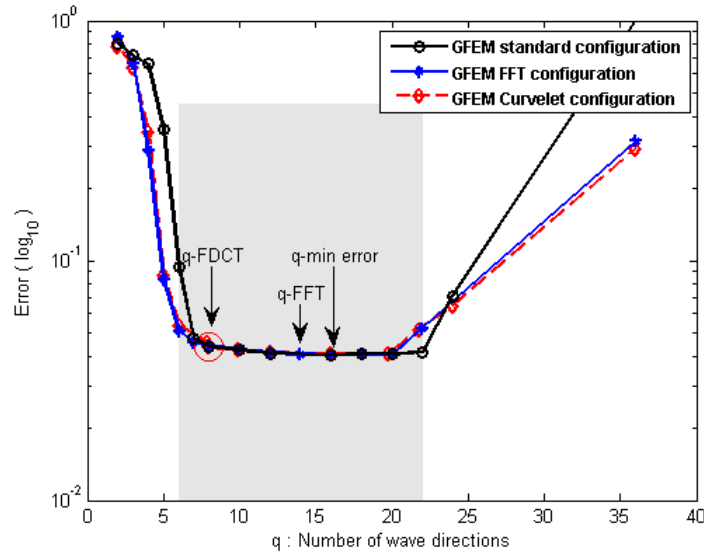
Fig. 4.20 Error vs number of wave directions in traditional GFEM, GFEM enriched by using DFT and FDCT

The shaded area in Fig. 4.20 is the acceptable area for the number of wave directions and is resulted from the FFT procedure section 4.2. That pre-processing method defines
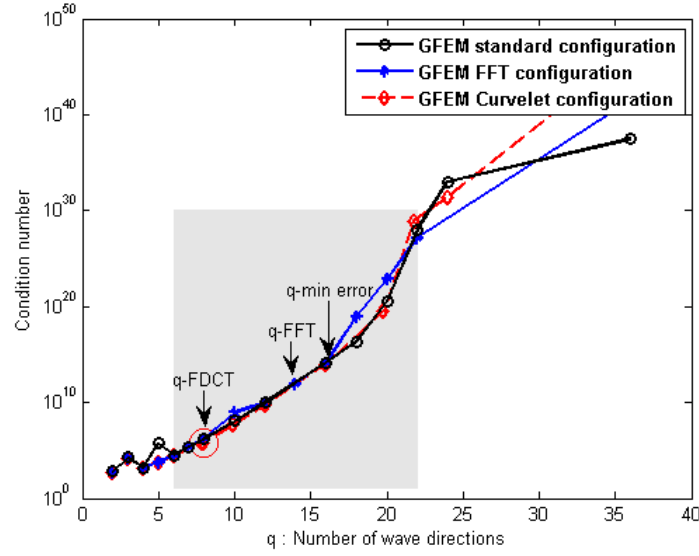
Fig. 4.21 Condition number vs number of wave directions in traditional GFEM, GFEM enriched by using DFT and FDCT

the maximum and minimum number of wave directions required to have qualified GFEM results. The minimum error in this range is related to q=16. However, the proposed methodology in this section defines $q = 8$ as the optimum number of wave directions that meets the limits and also leads to smaller condition number as shown in Fig. 4.21. The comparison between the quality parameters of GFEM solution for the two methods and also the GFEM solution with minimum error in this problem can be seen in table 4.3.

Table 4.3 Comparison of GFEM solution applying the FFT and FDCT and also GFEM with minimum error for the reflector problem with $\theta_i = 30^o$, $h = 0.4\lambda$

GFEM with	FDCT	FFT	Minimum error
Identified angles	[0 22 28 90 180 202 208 270]	[26 36 206 216 326]	—
Identified q	$q_{opt} = 8$	$6 \leq q \leq 22$	—
Proposed configuration	$q = 8$ θ_{max}=different for each node	$q = 14$ θ_{max}=26	$q = 16$ θ_{max}=standard distribution
NDOF	3408	5964	6816
Error	0.0436	0.0407	0.0406
Condition number	$6.72 * 10^5$	$8.52 * 10^{11}$	$1.39 * 10^{14}$
Running time(sec)	1132.70	2341.59	2649.450

As shown, the two mentioned methods achieved approximately the same error which is near to the minimum error of the GFEM solution of this problem. However, the condition number improved intensively by using 8 wave directions in the method using FDCT. Additionally, the GFEM with FDCT was 2.06 times faster than the GFEM with FFT and also 2.34 times faster than the GFEM with minimum error. Consequently, the pre-processing methodology using the FDCT is more efficient than the FFT and also the traditional GFEM.

Chapter 5

Conclusion and Future Work

5.1   Conclusion

In this work, it has been tried to develop some methodologies to improve the quality parameters of GFEM solution in problems with Helmholtz equations. In one view, the Discrete Fourier Transform was applied on the coarse mesh FEM solution of a problem in order to identify an effective distribution of the plane wave enrichment function of the GFEM. The main advantage of the proposed method is that it is able to identify suitable values for q using a pre processing systematic approach. It shows that, if q is selected between some limits and the directions are clustered considering the identified angles, good quality results can be achieved even using a small number of wave directions. Some case studies were presented as a proof of concept. The Generalized Finite Element simulations in free space and the L-shape reflector were carried out and it was demonstrated that the obtained results were in a good agreement with the idea proposed in this work. Results using the free space problem show that, for far field regions, only a pair of plane waves aligned with the direction of the propagation are necessary to lead to accurate solutions. For near the scattering regions, keeping equally spaced wave distributions can reduce the influence of the noise introduced by the low quality FEM solution in the identification of the most important waves. A simple approach was used to translate the DFT information into enrichment function directions that is quite invariant with the choice of the cutoff parameters. Results also demonstrated a good agreement with the extents for the number of enrichment functions proposed in this work. In addition, the multiple circular scatter problem is added to the research to express the capability of the proposed method to deal with more complex and various type of problems. Although the mentioned approach define

the range of q for the accurate GFEM solution, it lacks definition of the optimum number of wave directions in this range.

After that and in another approach, the new method for defining appropriate GFEM configuration has been represented. This approach, addressed the methodology to identify the best number of enrichment functions for GFEM solution. The procedure recognizes the directions which contribute most in each part of the problem by analyzing the curvelet coefficients of the image of coarse mesh FEM solution. Therefore the appropriate total number of wave directions, q_{opt}, is extracted and used in GFEM solution with the same mesh size. The results indicate that the GFEM system of equations using q_{opt} is faster than the traditional GFEM with q_{max}. Additionally, the comparison of the error and condition number amounts shows that for approximately the same error, GFEM with FDCT needs a smaller number of degrees of freedom, which consequently leads to a better condition number. Consequently, it has an efficient performance for solving many problems in both quality and cost criteria.

5.2   Future Works

This study could be expanded in many aspects since there are open problems that GFEM can be used to solve them such as treating different domains. This research is a first step that opens the new area of research in GFEM field solutions. The suggestions for the future works are as follows:

1. As it was mentioned before, the optimum number of wave directions was identified using image whitening which is some kind of visual inspection and made this part of the algorithm a bit heuristic. Therefore finding automatic procedure to identify the q_{opt} according analysis on the curvelet coefficients is required to improve the procedure and make it completely automatic. It needs more study about the feature extraction using curvelet or other transforms such as wavelet or contourlet transform.

2. Although the MATLAB code was developed to apply different enrichment functions distribution for each node in the mesh, this capability in software code have not been used by mentioned testing problem. Therefore, more complex problems with more different wave directions should be employed to investigate the effectiveness of different local configurations in the mesh and finally, development of a local approach to choose best q for each node.

3. It was shown that FDCT analysis is efficient in homogeneous domains. Neverthe-less, for domains with discontinuities, the capability of FDCT in improving the GFEM quality needs to be investigated. As a consequence, the domain with two or more mediums which have different frequencies could be used in order to fully exploit the multiscale nature of the curvelet transform. It should be noted that, this activity needs more study about border detection and treatment methods which have been used in curvelet coefficients analysis.

4. As it was mentioned before, the numerical integration in the GFEM equations was done using Gauss points approximations on domains meshed by triangular elements. Other types of elements or approximation methods can be used and their effects on improvement of quality of GFEM results, remain to be investigated.

5. The suggested approach in this report could be used with the methods of mod-ication in the traditional plane wave enrichment function which was explained in the work of Ricardo Adriano [32] . This combination would be resulted in reduction of the numerical dispersion and improvement of the overall quality of the solution.

References

[1] J.M.Melenk, "Finite element methods with harmonic shape functions for solving laplace equation," Master's thesis, University of Maryland, College Park, (Adviser: I. Babuska), 1992.

[2] I. Babuska, G. Caloz, and J. Osborn, "Special finite element methods for a class of second order elliptic problems with rough coefficients," SIAM J Numerical Analytical, vol. 31, p. 945–981, 1994.

[3] F. Ihlenburg, Finite element analysis of acoustic scattering. New York: Springer, 1998.

[4] I. Babuska and S. Sauter, "The pollution effect of the fem avoidable for the helmholtz equation considering high wave numbers," SIAM J Numerical Analytical, vol. 34:2, pp. 392–423, August 1997.

[5] R. Kechrouda, A. Soulaimani, Y. Saadb, and S. Gowda, "Preconditioning techniques for the solution of the helmholtz equation by the finite element method," Mathematics and Computers in Simulation, vol. 65, no. 4, pp. 303–321, 2004.

[6] J.M.Melenk, On generalized finite element methods. PhD thesis, University of Maryland, College Park, (Adviser: I. Babuska), 1995.

[7] J. Melenk and I. Babuska, "The partition of unity finite element method. basic theory and applications," Computational Methods in Applied Mechanics and Engineering, vol. 139, no. 1, pp. 289–314, 1996.

[8] L. Zhang, Generalized finite element method for multiscale analysis. PhD thesis, Texas A and M University, College Station,(Adviser: T. Strouboulis), 2003.

[9] I. Babuska, U. Banerjee, and J. Osborn, "On principles for the selection of shape functions for the generalized finite element method," Comput. Methods Appl. Mech. Engrg., vol. 191, p. 5595–5629, 2002.

[10] I. Babuska, U. Banerjee, and J. Osborn, "Survey of meshless and generalized finite element methods: A unified approach," Acta Numerical, vol. 12, p. 1–125., 2003.

[11] I. Babuska, U. Banerjee, and J. Osborn, "Generalized finite element methods – main ideas, results and perspective," International Journal of Computational Methods, vol. 1, p. 67–103, 2004.

[12] J. Dolbow, N. Moes, and T. Belytschko, "Discontinuous enrichment in finite elements with a partition of unity method," Comput. Methods Appl. Mech. Eng., vol. 36, p. 235–260, 2000.

[13] N. Sukumar, D. Chopp, N. Moes, and T. Belytschko, "Modeling holes and inclusions by level sets in the extended finite element method," Comput. Methods Appl. Mech. Eng., vol. 190, p. 6183 – 6200, 2001.

[14] C. Duarte, I. Babuska, and J. Oden, "Generalized finite element methods for three-dimensional structural mechanics problems," Computers and Structures, vol. 177, p. 215 – 232, 2000.

[15] O. Laghrouche, P. Bettess, and R. Sugimoto, "Analysis of the conditioning number of the plane wave approximation for the helmholtz equation," European Congress on Computational Methods in Applied Sciences and Engineering, 2000.

[16] P. Ortiz, "Finite elements using a plane-wave basis for scattering of surface water waves,," Phil. Trans. R. Soc. Lond.A, vol. 362, p. 525–540, 2004.

[17] R. Astley and P. Gamallo, "Special short wave elements for flow acoustics,," Comput.Methods Appl. Mech. Engrg., vol. 194, p. 341–353, 2005.

[18] E. Perrey-Debain, O. Laghrouche, P. Bettess, and J. Trevelyan, "Plane-wave basis finite elements and boundary elements for three-dimensional wave scattering," Philos. Trans. R. Soc. Lond. A, vol. 362, p. 561–577, 2002.

[19] C. Farhat, I. Harari, and L. Franca, "The discontinuous enrichment method," Comput. Methods Appl. Mech. Eng rg, vol. 190, p. 6455–6479, 2001.

[20] C. Farhat, I. Harari, and U. Hetmaniuk, "A discontinuous galerkin method with lagrange multipliers for the solution of helmholtz problems in the midfrequency regime," Comput. Methods Appl. Mech. Eng rg, vol. 192, p. 1389–1419, 2003.

[21] P. Rouch and P. Ladeve'ze, "The variational theory of complex rays: a predictive tool for medium-frequency vibrations," Comput. Methods Appl. Mech. Engrg, vol. 192, p. 3301–3315, 2003.

[22] H. Riou, P. Rouch, and P. L. ze, "Extension of the variational theory of complex rays to shells for medium-frequency vibrations," J. Sound Vib, vol. 272, pp. 341–360, 2004.

[23] T. Strouboulis, I. Babuska, and R. Hidajat, "The generalized finite element method for Helmholtz equation: Theory, computation and open problems," Computer Methods in Applied Mechanics and Engineering, vol. 195, pp. 4711–4731, July 2006.

[24] O. Laghrouche, P. Bettess, and R. J. Astley, "Modeling of short wave diffraction problems using approximating systems of plane wave," Int. J. Numer. Meth. Engng., no. 54, pp. 1501–1533, 2002.

[25] O. Laghrouche, P. Bettess, and J. T. E. Perrey-Debain, "Wave interpolation finite elements for helmholtz problems with jumps in the wave speed," Comput. Methods Appl. Mech. Eng rg, vol. 194, p. 367–381, 2005.

[26] T. Strouboulis, L. Zhang, and I. Babuska, "p-version of the generalized fem using mesh-based handbooks with applications to multiscale problems, equation: Theory, computation and open problems," Int. J. Numerical. Methods in Engineering, vol. 60, pp. 1639–1672, 2004.

[27] C. Lu and B. Shanker, "Hybrid boundary integral-generalized (partition of unity) finite-element solvers for the scalar Helmholtz equation," Magnetics, IEEE Transactions on, vol. 43, pp. 1002–10012, March 2007.

[28] T. Strouboulis, I. Babuska, and K. Copps, "The generalized finite element method: an example of its implementation and illustration of its performance," Int. J. Numerical. Methods in Engineering, vol. 47, p. 1401 1417, 2000.

[29] D. J. Kim, C. A. Duarte, and S. P. Proenca, "Generalized finite element method with global-local enrichments for nonlinear fracture analysis," Comput Mech, vol. 50, no. 563, 2012.

[30] C. Duarte and J. Oden, "An hp adaptive method using clouds," Comput. Methods Appl. Eng., vol. 139, p. 237 – 262, 1996.

[31] C. Duarte and J. Oden, "Hp clouds, an hp meshless method," Numer. Methods Partial Differential Equations, vol. 12, p. 673 – 705, 1996.

[32] R. Adriano, W. G. Facco, and E. J. Silva, "A modified plane wave enrichment to solve 2d electromagnetic problems using the generalized finite element method," IEEE Transactions on Magnetics, vol. 51, March 2015.

[33] A. Bovik, Handbook of Image and Video Processing. San Diego: Academic Press, 2000.

[34] E. Candès and D. Donoho, "Curvelets - a surprisingly effective non adaptive representation for objects with edges," Curve and Surface Fitting: Saint-Malo Proceedings and Larry L. Schumaker, Eds. Nashville, TN: Vanderbilt University Press, p. 1–10, 1999.

[35] E. J. Candès and D. L. Donoho, "New tight frames of curvelets and optimal representations of objects with piecewise c2 singularities," Communications on pure and applied mathematics, vol. 57, no. 2, pp. 219–266, 2004.

[36] E. Candès, L. Demanet, D. Donoho, and L. Ying, "Fast discrete curvelet transforms," Multiscale Modeling and Simulation, vol. 5, pp. 861–899, March 2006.

[37] T. Guha and Q. M. J. Wu, Curvelet Based Feature Extraction. intechopen: InTech, 2010.

[38] J. L. Starck, E. J. Candès, and D. L. Donoho, "The curvelet transform for image denoising," IEEE Transactions on Image Processing, no. 11, pp. 670–684, 2002.

[39] J.-L. Starck, M. Elad, and D. L. Donoho, "Image decomposition via the combination of sparse representations and a variational approach," IEEE Transactions on Image Processing, pp. 1570–1582, Oct 2005.

[40] J.-L. Starck, F. Murtagh, E. J. Candes, and D. L. Donoho, "Gray and color image contrast enhancement by the curvelet transform," IEEE Transactions on Image Processing, vol. 12, p. 706–717, 2003.

[41] T. Mandal, Y. Yuan, and Q. M. J. Wu, "Curvelet based face recognition via dimensional reduction," Signal Processing, vol. 89, pp. 2345–2353, December 2009.

[42] A. Majumdar, "Bangla basic character recognition using digital curvelet transform," Journal of Pattern Recognition Research, vol. 2, pp. 17–26, 2007.

[43] J. Zhang, S. Ma, and X. Han, "Multiscale feature extraction of finger-vein patterns based on curvelets and local interconnection structure neural network," Proc. ICPR, vol. 4, pp. 145–148, 2006.

[44] H. Al-Marzouqi and G. Al-Regib, "Curvelet transform with learning-based tiling," Signal Processing: Image Communication, vol. 53, pp. 24–39, 2017.

[45] S. Usama, M. Mofaddel, W. M. Abd-Elhafiez, and M. M. Abdel-Gawad, "Image object extraction based on curvelet transform," Applied Mathematics and Information Sciences, vol. 7, pp. 133–138, January 2013.

[46] A. Barnett and T. Betcke, "Mpspack user manual," Leibniz, and the Greatest Mathematical Clash of All Time (Thunder Mouth, New York, 2006), no. 1, 2013.

[47] Barnett, "Mpspack : 2d helmholtz scattering and eigenvalue problems via particular solutions and integral equations." https://github.com/ahbarnett/mpspack, 2013.